CATÓLICA
FACULTY OF BIOTECHNOLOGY

PORTO

Artificial Intelligence system for the automatic detection of Alzheimer's Disease using Magnetic Resonance Imaging (MRI)

by
Joana Rodrigues Silva

November 2021

CATÓLICA
FACULTY OF BIOTECHNOLOGY

PORTO

Artificial Intelligence system for the automatic detection of Alzheimer's Disease using Magnetic Resonance Imaging (MRI)

Thesis presented to Escola Superior de Biotecnologia of the Universidade Católica Portuguesa to fulfill the requirements of Master of Science Degree in Biomedical Engineering

by
Joana Rodrigues Silva

Supervisor: Prof. Doutor Pedro Miguel de Luís Rodrigues
Escola Superior de Biotecnologia, Universidade Católica Portuguesa

November 2021

Abstract

Alzheimer's disease (AD) is a neurodegenerative illness and is considered one of the main causes of dementia affecting millions of people. In its early stage – Mild-cognitive impairment (MCI) – is asymptomatic. Furthermore, although several studies have been made, until this day, no cure is yet available. Currently, some pharmaceuticals provide a slowing of symptoms if administered in early stages. However, to do so, the diagnosis needs to be properly performed to distinguish AD different stages. Thereby, there remains a growing need for early diagnosis to minimise AD impact by delaying it and its underlying effects. This work main purpose is to create an intelligent system that enables Alzheimer's automatic detection using Magnetic Resonance Imaging (MRI). To do so, a set of MRI images were analysed in the sagittal, coronal, and axial anatomical views and certain features were extracted and pre-selected to feed machine learning classic algorithms and a deep learning algorithm. On the one hand, for the Machine Learning classic algorithms, and for the comparison between: (1) AD vs Control (CN), a Bagged Trees Classifier reached a discrimination accuracy of 93.3%; (2) AD vs MCI, Quadratic SVM classifier got a discrimination accuracy of 87.7%; (3) CN vs MCI, Fine KNN and Subspace KNN classifiers achieved a discrimination accuracy of 88.2%, respectively; and (4) All vs All, the Subspace KNN classifier provided a discrimination accuracy of 75.3%. On the other hand, for the Deep Learning algorithm, and for the comparison between: (1) AD vs CN, a discrimination accuracy of 82.2% was achieved; (2) AD vs MCI, got a discrimination accuracy of 75.4%; (3) CN vs MCI, reached a discrimination accuracy of 83.8%; and (4) All vs All, reached a discrimination accuracy of 64.0%. In the CN vs MCI comparison, the proposed method, when compared with methods that use structural MRI (sMRI), showed an increase in classification accuracy of 9%. Therefore, the potential of this work in the diagnosis of AD, mainly in its early stages, is reinforced.

Keywords: Alzheimer's Disease, Mild-cognitive impairment, Magnetic Resonance Imaging, diagnosis, classic Machine Learning, Deep Learning.

Resumo

A doença de Alzheimer (DA) é uma doença neurodegenerativa que afeta milhões de pessoas, sendo considerada uma das principais causas de demência. A sua fase inicial - défice cognitivo ligeiro (DCL) – caracteriza-se por ser assintomática, e embora vários estudos tenham sido realizados, atualmente, ainda não existe uma cura disponível. No entanto, existem alguns medicamentos que proporcionam redução dos sintomas se administrados nas fases iniciais da doença. Contudo, para isto ser possível, o diagnóstico necessita de ser realizado corretamente, distinguindo-se as diferentes fases da doença. Deste modo, subsiste uma necessidade crescente de efetuar um diagnóstico precoce para minimizar o impacto da doença de Alzheimer, atrasando-a, bem como aos efeitos que lhe são subjacentes. Este trabalho tem como principal objetivo conceber um sistema inteligente que permita a deteção automática da doença de Alzheimer utilizando imagens de ressonância magnética (RM). Para tal, analisou-se um conjunto de imagens nos planos anatómicos sagital, frontal e horizontal, tendo sido extraídas e pré-selecionadas determinadas características para alimentar diferentes algoritmos clássicos de *Machine Learning* e de *Deep Learning*. Por um lado, para a técnica de *Machine Learning* clássica, e para a comparação entre: (1) Controlo (CN) vs AD, o classificador *Bagged Trees* atingiu uma precisão de discriminação de 93,3%; (2) MCI vs AD, o classificador *Quadratic SVM* obteve uma precisão de discriminação de 87,7%; (3) CN vs MCI, os classificadores *Fine KNN* e *Subspace KNN* atingiram uma precisão de discriminação de 88,2%, respetivamente; e (4) Todos vs Todos, o classificador *Subspace KNN* proporcionou uma precisão de discriminação de 75,3%. Por outro lado, para a técnica de *Deep Learning*, e para a comparação entre: (1) CN vs AD, foi alcançada uma precisão de discriminação de 82,2%; (2) MCI vs AD, obteve uma precisão de discriminação de 75,4%; (3) CN vs MCI, atingiu uma precisão de discriminação de 83,8%; e (4) Todos vs Todos, alcançou uma precisão de discriminação de 64,0%. Na comparação CN vs MCI, o método proposto, quando comparado com métodos que recorrem a RM estrutural, mostrou um aumento na precisão de classificação de 9%. Por conseguinte, é reforçado o potencial deste trabalho no diagnóstico da DA, principalmente nas suas fases iniciais.

Palavras-chave: Doença de Alzheimer, deficiência cognitiva leve, Ressonância Magnética, diagnóstico, *Machine Learning* clássica, *Deep Learning*.

Agradecimentos

Primeiramente, gostaria de expressar a minha gratidão ao meu orientador, Professor Doutor Pedro Rodrigues, por todas as oportunidades de aprendizagem proporcionadas, pela sua disponibilidade, orientação e por todo o apoio fornecido.

Aos meus pais, um sincero e desmedido obrigada, por serem um modelo de esforço e coragem. Pelo apoio e amor incondicional e por todos os valores transmitidos que se refletem no meu crescimento pessoal e profissional.

À Teresa, por acreditar em mim e me motivar nos momentos mais difíceis e de incerteza, por ter sido a minha companheira de trabalho ao longo desta etapa, pela paciência e pela ajuda que nunca deixou de existir.

Ao Telmo, Domingos, Miguel e Adriana, pela amizade, disponibilidade, preocupação e prontidão a ajudar.

À Raquel, por todo o carinho e compreensão, pela motivação e por todas as palavras de apoio que foram ditas em inúmeros momentos.

A toda a minha família, pelo carinho, motivação e momentos de descontração que me proporcionaram. Um obrigada especial ao meu avô Manuel que me inspirou e fez acreditar ainda mais na importância deste trabalho.

Joana

"If you are working on something that you really care about, you don't have to be pushed. The vision pulls you."

Steve Jobs

Outline

List of Figures

List of Tables

Acronyms and Abbreviations

Aβ	Amyloid-β
AD	Alzheimer's disease
ADA	Advanced Alzheimer's Disease
ADM	Moderate Alzheimer's Disease
ADNI	Alzheimer's Disease Neuroimaging Initiative
AlzNet	Alzheimer Network
ANN	Artificial Neural Network
APP	Amyloid Precursor Protein
Bior	Biorthogonal Wavelets
CAD	Computer-Aided Diagnosis
cMCI	converter MCI
CN	Control Subjects
CNN	Convolutional Neural Network
Coif	Coiflets
Cont	Contrast
Corr	Correlation
CSF	Cerebrospinal Fluid
DA	Doença de Alzheimer
DCL	Défice Cognitivo Ligeiro
Db	Daubechies wavelets
DL	Deep Learning
Dmey	Discrete approximation of Meyer wavelet
DNN	Deep Neural Network
DWT	Discrete Wavelet Transform
EEG	Electroencephalogram
EMCI	early MCI
Ener	Energy
Ent	Entropy

FC	Fully Connected
FDA	Food and Drug Administration
FDG-PET	Fluorodeoxyglucose Positron Emission Tomography
fMRI	functional Magnetic Resonance Imaging
Fk	Fejer-Korovkin wavelets
GLCM	Gray Level Co-Occurrence Matrix
GM	Grey Matter
GSS	Slice Selection Gradient
H	Hydrogen
Haar	Haar wavelet
Hom	Homogeneity
IACE	Inhibitors of Acetylcholinesterase
KNN	K–nearest neighbour
LMCI	late MCI
MCI	Mild Cognitive Impairment
MF	Median Filter
ML	Machine Learning
MMSE	Mini-Mental State Examination
MR	Magnetic Resonance
MRI	Magnetic Resonance Imaging
PCA	Principal Component Analysis
PET	Positron Emission Tomography
Rbio	Reverse Biorthogonal Wavelets
RBM	Restricted Boltzman Machines
RF	Radio Frequency
RM	Ressonância Magnética
ROIs	Regions of Interest
RROI	Rough Region of Interest
SD	Standard Deviation
sMCI	stable MCI
SVM	Support Vector Machine
Sym	Symlets
Var	Variance
WMHs	White Matter Hyperintensities
3D DenseNet	3D Densely Connected Convolutional Networks

CHAPTER 1

Introduction

1.1 Motivation

Nowadays, with technological advances in several areas, there is an increase in the average life expectancy worldwide, causing growth in individuals with age-related diseases. Alzheimer's Disease is a neurodegenerative disorder that partakes in a higher prevalence rate in older individuals, estimated to double every 5 years after age 65 [1].

AD, among other neurodegenerative diseases, has been the focus of many studies. However, until this day, no cure is yet available. In this sense, early diagnosis portrays a challenge for the scientific community. Additionally, it has been studied therapeutic solutions that resort to pharmaceuticals, delaying the progression of the symptoms. In advanced stages, the patient quality of life decreases as the need for continued care increases [2]. Therefore, it is imperative to find more precise and robust means of diagnosis, to minimise the disease impact by delaying its evolution.

Currently, several imaging techniques provide an in vivo diagnosis. More specifically, Structural Magnetic Resonance Imaging allows, in a non-invasive way, the anatomical and functional brain structures visualisation [3]. Thus, it supports a disease precise and early diagnosis as well as a measurement of its progression.

Furthermore, considering the dependence on the operator and time consumption caused by the manual process of reviewing each MRI, it is crucial to automatise it as much as possible. To that end, this work aims to find a diagnostic tool able to detect AD in its early stages to assist medical professionals.

1.2 Contributions and Objectives

The main purpose of this work is to develop an artificial intelligence system that enables AD automatic detection in its early stages by using MRI. In this way, the images were processed and decomposed employing the 2-D Discrete Wavelet Transform and features were extracted. Both classic Machine Learning and Deep Learning algorithms were used to classify and to obtain the distinction of the different study groups. In general, the accuracies obtained through this method are superior to certain state of the art studies.

1.3 Thesis Structure

This disseration is structured in six chapters. The first chapter presents the dissertation and contains all the aspects that motivated the present work execution and its fundamental contributions. The second chapter provides detailed information about Alzheimer's disease to understand and diagnose this illness. The third chapter focuses on Magnetic Resonance Imaging and the effects of this disease in the technique. Chapter four exhibits a detailed explanation of the methodology applied in this work. In chapter five, the results obtained in this work and their discussion are presented. Finally, in chapter six the conclusions and some future perspectives are described.

CHAPTER 2

Alzheimer's Disease

Alzheimer's disease is a progressive neurodegenerative illness and one of the leading causes of dementia, accounting for approximately 70%. This disease is characterised by gradual changes in the individual's memory and, consecutively, by the gradual impairment of various cognitive functions: language, executive functions, visual and temporospatial abilities, and praxis [2, 4]. In this chapter, AD will be explored in more detail, characterising it and approaching the alterations caused as well as means of diagnosis and treatment currently provided.

2.1 Epidemiology

According to [5], the prevalence rate of AD represents 5.3%, 13.8% and 34.6% for individuals aged 65–74, 75–84 and 85 or older, respectively and is estimated to double every 5 years after age 65 [1]. In this way, it is possible to state that age significantly affects the number of AD patients. In other words, an increase in average life expectancy will reflect an increase in this number. Further studies show that people aged 65 are at higher risk of AD. Besides that, younger people can develop the disease, although it is not as common [5].

From AD diagnosis until death, people aged 65 and older survive, on average, 4 to 8 years. Nonetheless, some people can live up to 20 years with the disease. This extended duration before death entails a significant impact on the public health as a considerable part of that period is spent in a state of dependence and disability [5].

Moreover, in 2006 the global number of AD carriers was accounted for 26.6 million, and it has been estimated that this number will increase. [1, 6]. Figure 2.1 displays the proportion of caregivers for people with AD and other dementias in comparison with other older people [5]. It is important to mention that a late-stage AD entails higher levels of care and thus a higher economic burden.

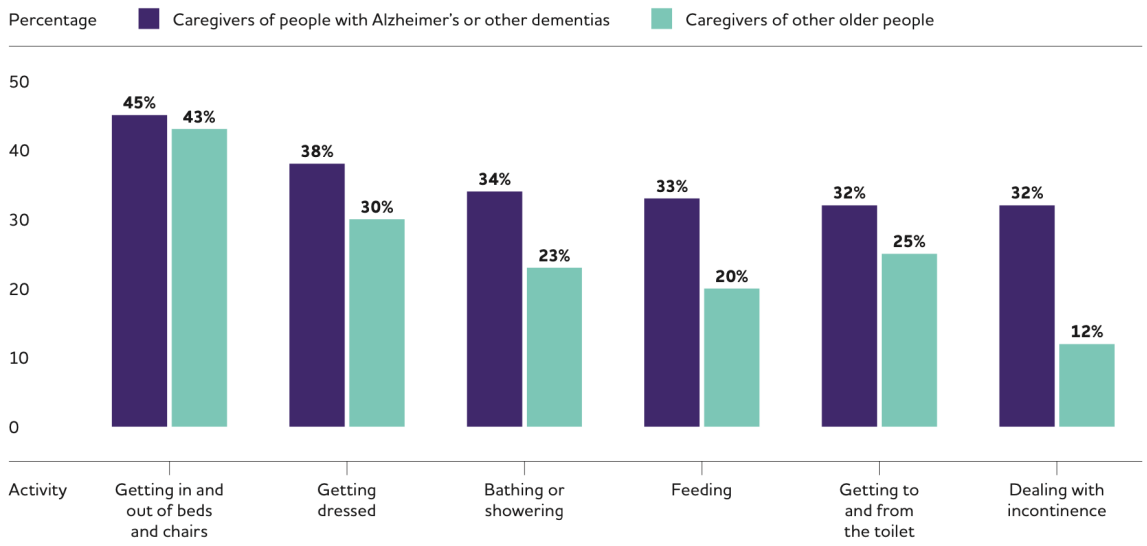

Figure 2.1: Caregivers of people with Alzheimer's and other Dementias in comparison with caregivers of other older people [5].

2.2 Neuropathological alterations

AD is associated with several characteristic neuropathological changes. Among them, formation of senile plaques and intraneural neurofibrillary braids, granulovacuolar degeneration and neural loss [2].

The formation of senile plaques and intraneural neurofibrillary braids are the main biomarkers related to AD. Senile plaques are spherical structures composed of a central nucleus and a crown of degenerative structures, axons, and synapses. Most of the central nucleus contains extracellular β-amyloid (Aβ) peptides, which are derived from a larger protein known as an amyloid precursor protein (APP) [2]. Aβ comes due to a sequential proteolytic cleavage of APP performed by β-secretase and γ-secretase. Usually, α-secretase cleaves APP inhibiting Aβ formation, but in AD this does not occur. Consequently, there is a progressive accumulation of abnormal levels of Aβ, leading to the formation of senile plaques [7, 8]. This accumulation interferes directly, through cytotoxic mechanisms, in the deterioration of synaptic terminals (reducing the level of acetylcholine), thereby initiating the pathological process of AD [2].

Concerning intraneural neurofibrillary braids, these are intracytoplasmic structures located in neurons and formed due to aggregates of abnormal levels of tau protein [2, 4].

In AD, due to the accumulation of extracellular β-amyloid, there is hyperphosphorylation of tau protein, resulting in tau aggregates. These aggregates produce twisted paired helical filaments known as neurofibrillary tangles that, in turn, lead to synaptic and neuronal dysfunction [4].

Figure 2.2 illustrates the main changes produced in the brain of an AD patient [9]. Memory and executive functions are related to hippocampal atrophy, as the senile plaques and the neurofibrillary

braids are predominantly found in the hippocampus. In general, AD patients suffer from global atrophy of the brain, resulting in a decreased brain volume [10, 11].

According to [5], a study has shown that the increased levels of β-amyloid in the brain start to appear 22 years before symptoms develop. Brain atrophy initiated 13 years prior to symptoms onset and glucose metabolism decreased 18 years before the symptoms began.

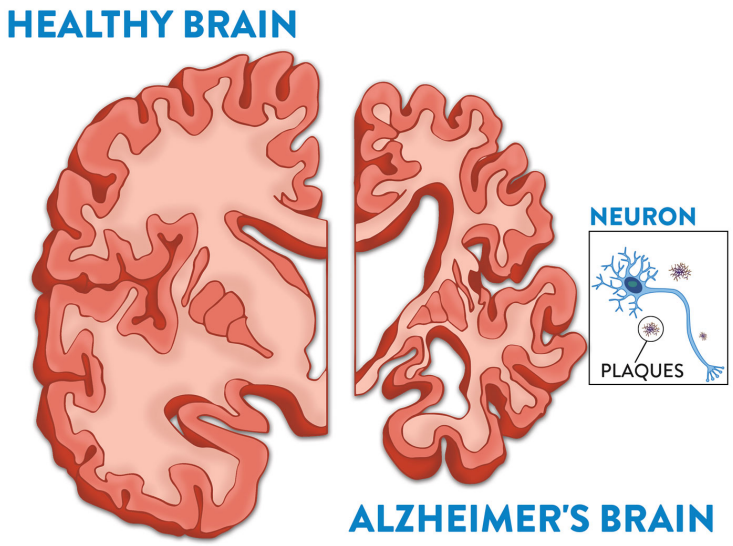

Figure 2.2: Changes produced in an AD patient brain [9].

2.3 Characterization

This disease can be divided into three phases, which differ in the level of perception of brain changes: pre-clinical AD, Mild Cognitive Impairment due to AD and Dementia due to AD. This last phase is separated into mild, moderate, and severe [2, 5].

The pre-clinical AD is distinguished by the asymptomatic period that occurs between the initial brain lesions and the appearance of the first symptoms. Meaning that, brain changes indicative of the first signs of AD have already occurred, however symptoms such as memory loss have not yet been expressed [5].

MCI is a pre-dementia state in which individuals have cognitive deficits greater than those that naturally emerge with age, but do not fit the criteria imposed for the diagnosis of AD. Not all patients with MCI develop AD, but studies suggest that the risk of developing AD is 15% in the first year and, approximately, 50% after 5 years [2, 5].

The last stage, Dementia due to AD, is characterised by severe symptoms. The mild phase corresponds to the period where the individual is still operational in several areas, but, for safety

reasons, may need help in certain activities. The moderate phase, which is longer, is distinguished by the difficulty in communicating and performing routine tasks, such as dressing and bathing [2, 5]. In the more severe and advanced stages of the disease, individuals require 24-hour care as damage to the areas of the brain responsible for movement emerge [5].

In brief, the primary symptoms of the disease include memory loss (the most severe and early symptom), agitation, depression, delirium, resistance to care, confusion in daily activities, obsession, apathy, sexual disinhibition, sleep disturbances and, lastly, psychosis [5].

2.4 Diagnosis and Treatment

The diagnosis of the disease can be performed in numerous ways. Usually, the main risk factors are pondered through physical and history examination from the individual and his family. Amongst the risk factors, the key ones include: age (as demonstrated in chapter 2.1), dementia family history (since a parent with AD quadruples the disease risk), Down Syndrome, mutations in the genes associated with AD (14-PSI, 1-PS2 and 21-APP chromosomes), and, lastly, ApoEe4 polymorphism, being this the principal factor in the late stages since it triples the risk in every age. There are some other risk factors considered likely, such as alcoholism, smoking, low scholarity, hypertension, type 2 diabetes, obesity, sedentary lifestyle, among others [2].

With these risks and through neurological and cognitive exams, it is possible to discard other causes of dementia and evaluate the stage of AD. The most common cognitive test is the Mini-Mental State Examination (MMSE), in which patients answer several questions regarding orientation, retention, attention and calculus, evocation and language [5, 12].

Additionally, state of the art exams can also be employed to identify both neurodegeneration and amyloid deposition. These exams include Magnetic Resonance Imaging, Positron Emission Tomography (PET), Electroencephalogram (EEG) and Cerebrospinal Fluid (CSF) Analysis. An overview on the state of the art covering some of the methods described bellow is displayed in Tables 2.1 and 2.2.

- **MRI:** There are two solutions available in what concerns MRI scans. On the one hand, structural MRI, which allows the visualization of changes in tissue characteristics as well as in the brain structure, for example, shrinkage of the brain and other vascular irregularities [13]. On the other hand, functional MRI (fMRI) measures, indirectly, neural activity through measurements of blood oxygen level-dependent Magnetic Resonance (MR) signal. It is used to study the functional integrity of the brain regarding several cognitive domains, for example, memory [3].

- **PET:** In this neuroimaging technique there are several methods, nonetheless the most frequently used corresponds to fluorodeoxyglucose positron emission tomography (FDG-PET) since glucose is the main source of the brain's energy. FDG-PET enables measurements of the acceptance

of radiolabelled glucose analogue which can be associated with synaptic activity and cerebral metabolism [3, 13].

- **EEG:** Through EEG signals analysis medical professionals can find determined abnormalities specific in patients with AD. From these abnormalities, three can be distinguished: EEG synchrony disturbance, reduced complexity of the EEG signals and slowing of the EEG signals [14].
- **CSF:** Chemistry has been targeted in several investigations in the search of AD biomarkers since it is found in direct contact with the extracellular space of the brain. Nowadays, three different CSF biomarkers are evaluated: the level of abnormally hyperphosphorylated tau protein, the concentration levels of the total amount of tau protein and, lastly, the 42 amino acid isoforms of β-amyloid peptide, Aβ42 [15].

Regarding the treatment available for AD, there are two possible methods: drugs and non-pharmacological interventions [2].

In terms of drugs, the inhibitors of acetylcholinesterase (IACE) and the modulators of glutamate receptors are, commonly, administered. Since Alzheimer displays a decline in acetylcholine, IACE drugs enable neurotransmitters to be more available in the synaptic pathway. In addition, modulators of glutamate receptors allow the improvement of synaptic transmission. This drug demonstrates better results in moderate and advanced stages since it reduces behavioural and psychologic symptoms. Concerning non-pharmacological interventions, it can be divided into three groups: cognitive approaches, memory exams and therapeutical approaches (for more severe cases). In this last approach, stimulation activities, validation and orientation towards reality therapies, among others are performed [2].

Table 2.1: Overview on State of the Art Studies

Study	Accuracy	Methodology
[16]	CN vs AD - 85.86% (1)	Ruiz *et al.* propose an automatic computer-aided diagnosis (CAD) system using MRI images. It was created an algorithm that proceeds to extract features from regions of interest (ROIs) for both the identification of AD patients and forecasts the severity of AD effects on these regions. In this work, different classifiers were tested for each comparison to distinguish the ones with a superior discriminative power. The best results were found when using (1) VAF-FS (2) RF and (3) XGBoost.
	CN vs MCI - 71.92% (2)	
	MCI vs AD - 68.92% (3)	
[17]	CN vs AD - 99.2%	The authors studied the need to associate neuropsychological tests, in this particular case Mini-Mental State Examination (MMSE), with MRI, for the classification of different stages of AD. In this work, different classifiers were tested for each comparison for both hypothesis with or without the MMSE. It was concluded that combining the MMSE with other features, such as hippocampus left and right volume, improves the classification of AD.
	CN vs MCI - 78.5%	
	MCI vs AD - 91.3%	
[18]	CN vs AD - 99.14%	Jain *et al.* apply a mathematical model PFSECTL developed by performing transfer learning using a Convolutional Neural Network (CNN) architecture (VGG-16), to establish a 3-way classification CN vs MCI vs AD. The model obtained is subsequently trained on the most informative brain MRI slices, whilst maintaining the layers of the base model non-trainable.
	CN vs MCI - 99.22%	
	MCI vs AD - 99.30%	
	CN vs MCI vs AD - 95.73%	
[19]	CN vs AD - 96.25%	In this paper, it was studied the reliability of two different CNN architectures, VGG and Inception, in an AD diagnosis through transfer learning methods with a smaller training size. Both VGG and Inception were initialized with pre-trained weights from large datasets and the fully connected layer was re-trained with a smaller one. It was found that with this method it is possible to obtain comparable or better results with a smaller training size.
[20]	CN vs AD - 96.70%	The authors used AD patients' functional magnetic resonance imaging (fMRI) images, as well as their MMSE scores. In this work, both machine learning and CNN architecture are used. The feature extraction of the input layers is performed by robust multitask methods and then reduced by means of the PCA method. Several classification methods were tested, but CNN arquitcehture achieved better results.
[21]	CN vs AD - 99.30%	In this study a deep learning methodology was employed to discriminate between AD and CN patients from 2D anatomical slices collected using MRI. It was used a CNN architecture with the 2D slices as input with the aim of extracting the deep network weightings, named as Alzheimer Network (AlzNet). The effect of several parameters on AlzNet were evaluated using different performance metrics.

Table 2.2: Overview on State of the Art Studies (continuation)

Study	Accuracy	Methodology
[22]	CN vs AD - 88.9%	Liu *et al.* propose a deep learning structure established on CNN for classification of AD and joint automatic hippocampal segmentation through structural MRI images. With the aim of performing the disease stages classification, it was developed a multi-task CNN model followed by a 3D Densely Connected Convolutional Networks (3D DenseNet) to extract and combine features of the 3D patches obtained in the hippocampal segmentation.
	CN vs MCI - 76.2%	
[23]	CN vs AD - 96,8%	The authors used deep learning methods to define distinctive AD signatures from several inputs, such as MRI images, gender, age and MMSE scores. To perform a disease classification, it was used a convolutional network that creates high resolution maps of disease probability from local brain structure to a multilayer perceptron.
[24]	CN vs AD - 87.39%	This paper proposes a new feature extraction method: Rough Region of Interest (RROI), for texture analysis on segmented data. The algorithm selects specific image blocks and computes their textures which are then introduced in feature selection algorithms to choose the ones with higher relevance.
	CN vs MCI - 64.74%	
	MCI vs AD - 63.41%	
	cMCI vs sMCI - 66.38%	
[25]	CN vs AD - 92.85%	Maqsood *et al.* resort to transfer learning with the intention of classifying Alzheimer's Disease by perfecting a pre-trained convolutional network, AlexNet. This architecture is both trained and tested over pre-processed segmented and un-segmented MRI images for multi-class and binary classification. The algorithm exhibited better results for multi-class classification of un-segmented images.
	CN vs MCI vs AD - 89.66%	
[26]	CN vs ADM - 95.99%	The authors propose a new electroencephalogram (EEG) signal processing tool, Lacsogram. Lacstral and Cepstral distances between subbands are used to extract measures to discriminate and characterize AD in the different stages and for comparison, respectively. The several binary classifications were achieved with an artificial neural network,ANN.
	CN vs MCI - 98.06%	
	MCI vs ADM-ADA - 93.85%	
	All vs All - 95.55%	
[27]	CN vs AD - 96.8%	In this paper a deep neural network (DNN) is proposed to detect AD in early stages by means of the grouping of MRI, Positron Emission Tomography (PET) and neuropsychological test scores. MRI and PET features extracted (training set) and selected (test set) perform as inputs to the DNN. The algorithm performs binary and multiclass classifications.
	CN vs EMCI - 84.0%	
	CN vs LMCI - 84.1%	
	EMCI vs LMCI - 69.5%	
	EMCI vs AD - 90.3%	
	LMCI vs AD - 80.2%	

cMCI – converter MCI; sMCI – stable MCI; ADA – Advanced Alzheimer's Disease; ADM – Moderate Alzheimer's Disease; EMCI – early MCI; LMCI – late MCI

CHAPTER 3

MRI: Imaging Technique

Imaging techniques are used as non-invasive means for AD diagnosis and prognosis. The imaging modalities are currently focusing on the identification of amyloid deposition or neurodegeneration. More specifically, MRI promotes the in vivo visualisation of the anatomical and functional structures of the human body with high resolution and contrast [3]. In this chapter, this imaging technique will be reviewed and the effects AD has upon it will be explored.

3.1 MRI Principles

Magnetic resonance is supported by the interaction conducted between a nucleus and an applied magnetic field. Considering that the human body is mainly composed of water and fat (tissues containing hydrogen, H), the H nucleus is chosen to examine the human body through MR techniques [28].

In an arbitrary volume of tissue with hydrogen atoms, every proton is characterized as having an equal magnitude spin vector. Nonetheless, the spin vectors contained in every proton within the tissue are randomly oriented, meaning that if a vector addition of these spin vectors was executed, the sum result would be zero, i.e., the tissue magnetization network does not exist [28].

Conversely, if the tissue is positioned inside a magnetic field B_0, the individual protons initiate perpendicular rotation and precess about it. The precession phenomena occurs due to the interaction of the magnetic field with the nucleus's spinning positive charge, as shown in Figure 3.1 [29].

The rate or frequency of precession is proportional to the strength of the magnetic field, and it can be conveyed by the Larmor equation, equation 3.1:

$$w_0 = \gamma \frac{B_0}{2\pi} \tag{3.1}$$

where, w_0 is the Larmor frequency (MHz), B_0 the magnetic field strength (T), and γ the gyromagnetic ratio $(s^{-1}T^{-1})$ [28].

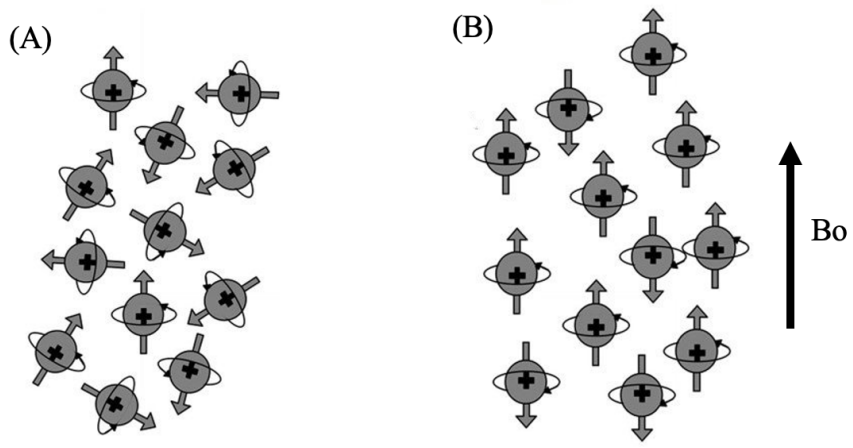

Figure 3.1: (A) Without an external magnetic field the spin vectors are randomly oriented. (B) With an external magnetic field, B_0, applied, the spin vectors align parallel or antiparallel to B_0 [29].

Once protons absorb the energy from the radio frequency (RF) pulse (resultant of the transmission of photons at Larmor frequency), its spin transfers to a higher energy level, which will force it to rotate. Protons return to their equilibrium state when the RF pulse ceases, making them release the absorbed energy. This effect is referred to as relaxation. Relaxation is an essential process in MR since it presents the main mechanism for image contrast. Relaxation times are measured for grey matter or cerebrospinal fluid and can be distinguished in T1 and T2 [28].

3.2 Clinical Magnetic Resonance Imaging

There are three physical gradients used, one in each x, y, and z directions. These physical gradients are allocated to "logical" or functional gradients (which are mandatory to acquire an image) such as phase encoding, slice selection and readout or frequency encoding. This allocation is arbitrary and differs according to the patient positioning, the manufacturer's choice of physical directions and the acquisition parameters. The aggregation of the data sampling period, the pulse gradients, the RF pulses, and the period between each image acquisition is acknowledged as a pulse sequence [28].

Larmor's equation states that the frequency absorbed is proportional to the magnetic field B_0, but with the presence of magnetic field gradients, this equation is expanded, equation 3.2:

$$w_i = \gamma(B_0 + G \cdot r_i) \tag{3.2}$$

where, w_i is the frequency of the proton positioned at r_i and G is a vector representative of the total gradient amplitude and direction [28].

The MRI image is a frequency and phase map of protons generated by single magnetic fields in the given image. The resulting image contains a set of pixels (digital picture elements) representative of voxels (volume elements of tissue). The intensity of each pixel is proportional to the number of protons within the voxel, induced by the T1 and T2 relaxation times for tissues within the voxel [28]. Meaning that areas with lower water content (fewer hydrogen protons) emit signals back to the RF coils, resulting in different shades of grey that reflect different densities. Thereby, areas with more hydrogen protons will be lighter (for example, fat), and with fewer hydrogen protons will be darker (for example, dense bone) [30].

3.3 Slices Selection

In MRI, it is firstly located the RF excitation to a region of space through the frequency-selective excitation in combination with the slice selection gradient, G_{SS}. The slice orientation is determined by this gradient direction. Both the slice thickness and position are determined by the gradient amplitude in conjunction with certain RF pulse characteristics [28]. The resulting slices can be seen in Figure 3.2.

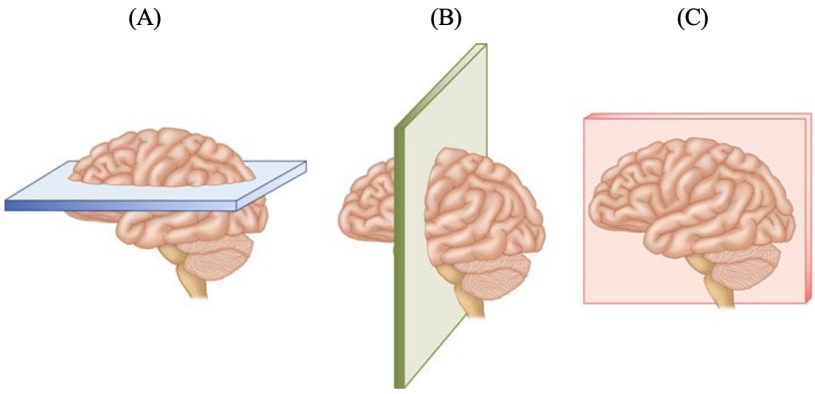

Figure 3.2: Different slices of the human brain: (A) Axial plane (B) Coronal plane (C) Sagittal plane [31].

An RF pulse can be divided into two parts regarding its frequency: a central frequency and bandwidth or a narrow range of frequencies. Thus, diverse positions of the slices can be obtained

through changes in the central frequency. Additionally, the thickness of the slice is determined by the G_{SS} and the frequency bandwidth. Having in mind that, normally, the bandwidth is fixed to a given value, only changes in the G_{SS} amplitude can vary the slice thickness. Meaning that, a larger G_{SS} provides a smaller slice thickness [28].

3.4 Alzheimer's Disease Effects in Magnetic Resonance Imaging

In the case of AD, structural MRI allows for atrophy and changes in tissue measurements [13]. MRI-based atrophy measurements are considered valid markers of disease state and progression since atrophy seems to be an inevitable and intrinsic factor of progressive neurodegeneration. Besides that, changes in structural measures, such as ventricular enlargement, hippocampus, entorhinal cortex, whole brain, and temporal lobe volumes, can be associated with modifications in cognitive performance [30]. To entail that MRI can reliably detect AD in the MCI stage, one of the subsequent three markers are necessary: abnormal neuronal CSF markers (Aβ and tau protein), temporoparietal hypometabolism and, lastly, atrophy in medial temporal lobe structures (entorhinal cortex and hippocampus) [32, 33]. In comparison with controls, and at the mild dementia stage of AD, the hippocampal volumes are reduced by 15–30% and entorhinal cortex volumes by 38–40%. Regarding hippocampal atrophy, its presence is specifically associated with deficits in memory and executive functioning in AD patients. Throughout the progression of the disease, atrophy spreads to other areas, which leads to grey matter (GM) losses resulting in cognitive dysfunction. Additionally, patients with AD exhibit greater white matter hyperintensities (WMHs), which correlates with hippocampal atrophy (as shown in Figure 3.3). In general, atrophy progression assessed by MRI is being widely used as an efficiency and safety outcome measure in clinical trials. Nonetheless, out of all the MRI markers, AD hippocampal atrophy is pondered as the best established and validated [32, 33].

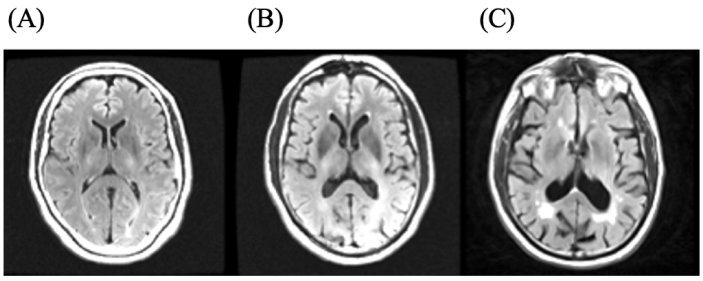

Figure 3.3: Brain changes assessed in (A) control (B) MCI and (C) AD patients by MRI [33].

CHAPTER 4

Methodology

4.1 Data Base Characterization

The MRI scans images were obtained from the Alzheimer's Disease Neuroimaging Initiative (ADNI) database (for downloat at http://adni.loni.usc.edu [34]). All the subjects had a standardized protocol from three different imaging vendors (GE Healthcare, Philips Healthcare or Siemens) where the scan time overall was about 45 minutes per subject and session. Each exam undergoes quality control, so that in case of, for example, subject motion or poor anatomic coverage, the scan is considered unusable. The database consists of 89 subjects scanned longitudinally at 3T with a 3-year follow-up, in which 24 are healthy control subjects, 44 are MCI patients and 21 are AD patients. Demographic data of the three groups is summarized in Table 4.1.

Table 4.1: Overview of the database.

Diagnosis	# subjects	Media ± SD	Age Range	Gender		MMSE Average ± SD
				F	M	
AD	21	76.2 ± 8.34	59 - 89	14	7	19.81 ± 6.46
MCI	44	73.8 ± 8.92	56 - 90	10	34	24.52 ± 2.91
CN	24	78.2 ± 4.64	71 - 88	14	10	29.50 ± 0.66

4.2 Introduction to the Pre-Processing Techniques

4.2.1 Image Level Adjustment

Image level adjustment is a technique used to adjust the intensity value of a given image to a specific range by linearly stretching the pixel level of an image. In this way, it is possible to increase

its contrast [35]. The linear level adjustment is performed according to the following equation 4.1. To make these modifications, the Matlab® function *imadjust* can be used. This function maps the intensity values of the grayscale images so that 1% of data on top and bottom pixel values is saturated, respectively. This procedure will increase the contrast of the output image which is of the same size as the original grayscale image containing the mapped values [35, 36].

$$p_{adjust}(m,n) = Bottom + \frac{p(mn)-L}{H-L} * (Top - Bottom) \quad (4.1)$$

where, $p_{adjust}(m,n)$ is the output image pixel, $p(m,n)$ is the input image pixel, H the maximum pixel level in the original image, L the minimum pixel level in the original image, Top the maximum pixel level in the desired image, and $Bottom$ the minimum pixel level in the desired image [35].

4.2.2 Median Filter

The median Filter (MF) is a sliding-window nonlinear smoothing process. It is performed to remove different types of noises, but it is considered most effective at reducing salt and pepper noises [35, 37]. The principle on which the MF is based on consists of replacing the gray level of each pixel by the median of the gray levels in a neighbourhood of pixels [35]. In other words, the MF window goes through each image pixel and the median intensity value replaces the window's center in the filtered image. Usually, to preserve the edges, the image boundaries are padded with zeros [37]. The standard MF is given by equation 4.2:

$$Y_i = med(W_i) = med(X_i + r), r \in W \quad (4.2)$$

where, X_i and Y_i are the input and the output at location i of the filter. The pixels in window W_i can be represented by $X_i + r$, for $r = 1,\ldots,$ 2N+1. By default the window size is 3x3 [38].

It is a well-known fact that MF performs better than, for example, the mean filter. Thus, it is stated that MF can be more stable and robust than other filters available. Due to these factors, this filter is used as a foundation when developing more advanced image filters [35].

4.3 Introduction to the Processing Techniques

4.3.1 Discrete Wavelet Transform

The wavelet transform enables the analysis of signals or images at different scales or resolutions. It can be applied in two domains, the continuous and the discrete, in which each of them is composed

from the mother wavelet, denoted by ψ(t), by means of scale (s) and translation (τ) parameters in time domain [39, 40].

The discrete variation, Discrete Wavelet Transform (DWT) was chosen to describe the input images, since it is possible to maintain higher resolution at low-frequency bands [41]. It can be obtained by restraining both parameters to a discrete lattice with $s = 2^{-m}$ and $\tau = n \cdot 2^{-m}$, where m and n are integers. Hence, for a discrete-time signal $f(n)$, the wavelet decomposition on I octaves is given by,

$$f(n) = \sum_{i=1 to I} \sum_{k \in Z} c_{i,k} g[n - 2^i k] + \sum_{k \in Z} d_{I,k} h_I[n - 2^I k] \tag{4.3}$$

where, $c_{i,k}$ and $d_{I,k}$ corresponds to the coefficients of approximation component and coefficients of detail component, respectively [39, 42]. These coefficients are given by,

$$c_{i,k}(n) = \sum_n f(n) g_i^*[n - 2^i k] \tag{4.4}$$

$$d_{i,k}(n) = \sum_n f(n) h_I^*[n - 2^I k] \tag{4.5}$$

where, the parameters i and k indicate the wavelet scale and translation factors, respectively. Besides that, g_i characterize the coefficients of the low-pass and h_I the coefficients of the high-pass filters. Every wavelet type and family are different in what regards these filters. Section 4.3.1.2 presents an explanation on these families [39, 40].

4.3.1.1 DWT in Two Dimensions

When it concerns images, the DWT is applied to each dimension independently. Meaning that, rows and columns are treated as a signal, and, separately, put through the 1D DWT to build up to the 2D DWT [41].

Regarding to the first level of decomposition two transforms are applied, the horizontal and vertical transform. The horizontal transform is the first step in which each row is wavelet transformed and scaled, resulting in two half images (one with scaling coefficients, L, and the other with wavelet coefficients, H). The vertical transform is the second step in which both these coefficients are applied on each column of the previous two half images, resulting in four quarter sized images with a set of four sub-bands at each level (LL – low low, LH – low high, HL – high low, HH – high high), Figure 4.1 (c). Of these, three correspond to horizontal (HL), vertical (LH) and diagonal (HH) details [37][39]. The decomposition into four sub-bands is shown in Figure 4.1 (a).

For the second level decomposition, the steps mentioned above are reproduced on the LL image.

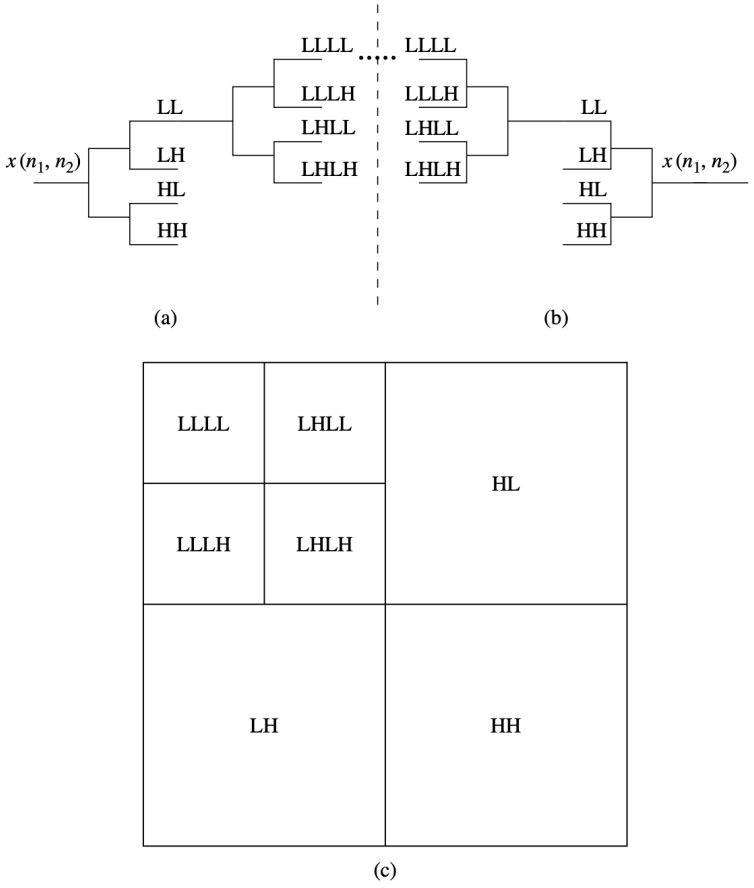

Figure 4.1: Implementation of wavelet image decomposition: (a) wavelet decomposition of input image $x(n1,n2)$; (b) reconstruction of $x(n1,n2)$; (c) nomenclature of sub-bands for a 3-level decomposition [43].

4.3.1.2 Wavelet Families and Subfamilies

A large number of wavelet families and subfamilies can be used for both discrete and continuous analysis. Nevertheless, for the present work only eight wavelet families were tested: Haar wavelet, Daubechies wavelets, Symlets, Coiflets, Biorthogonal wavelets, Reverse biorthogonal wavelets, Discrete Meyer wavelet and Fejer-Korovkin wavelets. Apart from the Haar and Discrete Meyer wavelet, each of them has subfamilies, for example, Daubechies express an order of N = 1,2, 3, . . . , 45 and Coiflets an order of N = 1, 2, 3, 4 and 5 [44–46].

The wavelet families differ in various properties, such as symmetry, regularity of the wavelet (smoother wavelets enable sharper frequency resolution), number of vanishing moments (an increase

in this number results in inadequate representations for a large class of signals and images). In Table 4.2, some of the properties of the wavelet families are detailed [44–46].

Table 4.2: Overview of the wavelet families properties.

Properties	**Wavelet**							
	Fk	**Sym**	**Db**	**Coif**	**Rbio**	**Bior**	**Dmey**	**Haar**
Orthogonal Analysis	X	X	X	X		X		X
Biorthogonal Analysis		X	X	X	X	X		X
Infinitely Regularity								
Arbitrary Regularity	X	X	X	X	X	X		
Continuous Transform	X	X	X	X	X	X		X
Discrete Transform	X	X	X	X	X	X	X	X
Fast Algorithm	X	X	X	X	X	X	X	
FIR Filters	X	X	X	X	X	X	X	X
Exact Reconstruction	X	X	X	X	X	X		X
Symmetry					X	X	X	X
Asymmetry	X		X					
Near symmetry		X		X				
Existence of φ	X	X	X	X	X	X		X
Arbitrary Number of Vanishing Moments		X	X	X	X	X		

4.3.2 Feature Extraction

Features are an important form of information when studying the structure of control and abnormal brain MRI images.

Gray level co-occurrence matrix (GLCM) is a statistical method that considers the spatial relationship of pixels and is employed to describe the texture of an image. It calculates the regularity with which pairs of pixel (with defined values and in a certain spatial relationship) appear on an image. More specifically, the number of rows and columns of a GLCM is the same as the gray levels on the image. Then, the co-occurrence matrix is created in four spacial orientations (0°, 45°, 90°, and 135°), and an additional matrix is set as the average of preceding matrices. With this information, a matrix is created, and four statistical measures are extracted (Contrast, Correlation, Energy and Homogeneity). Additionally, other texture metrics can also be obtained, such as Entropy, Variance, Standard Deviation, among others [47, 48].

The following table 4.3 indicates and summarises information about all the statistics mentioned [47, 48]. In this, each element i, j represents the frequency by which pixel with gray level i is spatially

related to pixel with gray level j and $P_{i,j}$ corresponds to the co-occurrence matrix with an NxN size [47].

Table 4.3: Features overview.

Feature	Formula	Description
Contrast	$\sum_{i,j=0}^{N-1} P_{i,j}(i-j)^2$	Measures the local variations between pixels
Correlation	$\sum_{i,j=0}^{N-1} P_{i,j}\left[\frac{(i-\mu_i(j-\mu_j))}{\sqrt{\sigma_i^2\sigma_j^2}}\right]$	Estimates the combined probability occurrence of the indicated pixel pairs
Energy	$\sum_{i,j=0}^{N-1} P_{i,j}^2$	Specifies the sum of squared elements in the GLCM
Homogeneity	$\sum_{i,j=0}^{N-1} \frac{P_{i,j}}{1+(i-j)^2}$	Measures the nearness of the distribution of elements in the GLCM to the GLCM diagonal
Entropy	$\sum_{i,j=0}^{N-1} P_{i,j}(-lnP_{i,j})$	Assesses the randomness of an intensity image
Variance	$\sigma_i^2 = \sum_{i,j=0}^{N-1} P_{i,j}(i-\mu_i)^2$, $\sigma_j^2 = \sum_{i,j=0}^{N-1} P_{i,j}(j-\mu_j)^2$	Measures the dispersion of the elements of an image
Standard Deviation	$\sigma_i = \sqrt{\sigma_i^2}$, $\sigma_j = \sqrt{\sigma_j^2}$	Measures the dispersion of the elements of an image and is the square root of variance

4.3.3 F-score

F-score is a simple supervised feature selection method established on a statistical methodology [49, 50]. This method allows the distinction of relevant features by measuring each feature individually, resulting in F-score values [50]. Having into consideration the within class and between class variances, the F-score can be calculated according to the following equation 4.6:

$$f-score(f_i) \quad = \quad \frac{\sum_j \frac{n_j}{c-1}(\mu_j-\mu)^2}{\frac{1}{n-c}\sum_j (n_j-1)\sigma_j^2} \tag{4.6}$$

in which, f_i corresponds to a given feature, n_j indicates the number of instances from class j, μ the mean feature value, μ_j the mean feature value on class j and σ_j the standard deviation of feature value on class j [50]. In this way, a higher F-score value entails a feature with a larger discriminatory power [49].

4.4 Machine Learning (ML) Algorithms

Machine Learning is a field of artificial intelligence in which machines perform their assignments using intelligent software. Thus, its purpose is to study and improve mathematical models that can be trained with data related to the context to make important decisions without full knowledge of every influencing elements [51].

4.4.1 Support Vector Machine

Support Vector Machine (SVM) is a machine learning classic classification algorithm that organizes data in a plane and resorts to the establishment of a decision boundary between two classes [52, 53]. This decision boundary maximizes the distance amongst the two classes by selecting the closest data points (support vectors) from each of them, Figure 4.2 [52]. Thereafter, the algorithm draws two lines, one for each class, and, in between, the maximizing function is traced, known as the hyperplane [53].

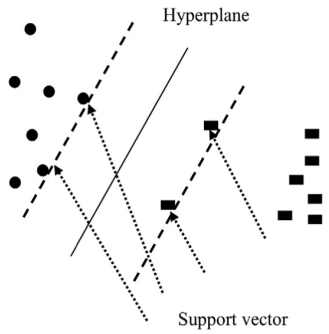

Figure 4.2: Classification process of a SVM [52].

For a multi-dimensional classification, the usual dimensional space is not effective, thereby a nonlinear methodology is used to classify the classes. To do so, SVM employs a kernel function that allows the mapping of the separation of higher dimensional data [54]. The linear kernel function and the polynomial kernel function are given by equations 4.7 and 4.8, respectively:

$$K(x_i, x_j) = x_i^T x_j + C \tag{4.7}$$

$$K(x_i, x_j) = (\gamma x_i^T x_j + r)^d \tag{4.8}$$

where, x_i and xj are the input vectors, C is an optional constant and γ, r, d are Kernel parameters (γ>0) [54].

4.4.2 K – Nearest Neighbour

K–Nearest Neighbour (KNN) is established on statistical data and one of the simplest classification algorithms [55, 56]. This classifier can be used on multi-class situations and makes a decision based on the training items in the training phase [56]. The testing feature vector is classified by determining the K–Nearest training neighbour vector and then the un-classified testing feature vector is assigned to the class with majority of K–Nearest training vector. Thereby, the implementation of KNN is centred on two parameters: the value of K that indicates the count of neighbours to be pondered and the distance between the testing and training vector. This last parameter is calculated by different metric measurement techniques [55, 56]. In this work, the Euclidean and Minkowski distances were used and can be calculated by the following equations 4.9 and 4.10, respectively [55, 57]:

$$d(a,b) = \sqrt{\sum_{i=1}^{n}(a_i - b_i)^2} \tag{4.9}$$

$$d(a,b) = (\sum_{i=1}^{n}|a_i - b_i|^{\frac{1}{p}})^p \tag{4.10}$$

4.4.3 Ensemble

Ensemble learning methods are based on the extraction of a set of features with several transformations. According to these features, learning algorithms are used to generate poor predictive results. Lastly, the ensemble learning algorithm combines results with numerous voting mechanisms so that enhanced performances, in comparison with other algorithms alone, are obtained. In other words, the predictive performance of a single model is improved by training different models and aggregating their predictions. When generating an Ensemble method two principles need to be considered: diversity (the participating inducers should be sufficiently diverse) and predictive performance (should be as superior as possible and at the same level as a random model) [58]. The most popular ensemble classification methods include: AdaBoost, Bagging, Gradient boosting, Random Forest, and Random subspace [58, 59]. A framework of the method is shown in Figure 4.3.

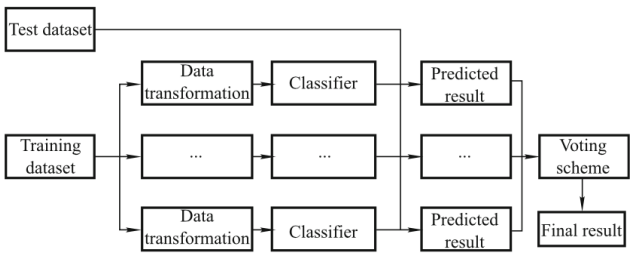

Figure 4.3: Framework of Ensemble Classification [59].

4.5 Deep Learning (DL) Algorithm

Deep Learning is a subfield of machine learning and a specific class of ANN that resembles the functioning of the human brain [60, 61]. DL contains several variants such as, autoencoders, restricted Boltzmann machines (RBM), and Convolutional Neural Networks [60]. In this work, the last variant was employed.

4.5.1 Convolutional Neural Networks

CNN's architecture is the most noticeable category of neural networks that is composed of multiple layers of neural computing connections: an input layer, output layer and many hidden layers, for example, convolutional, activation, pooling and fully connected (FC) layers, as exhibited in Figure 4.4. The input layer contains the image data that will then be classified in the output layer [60, 62].

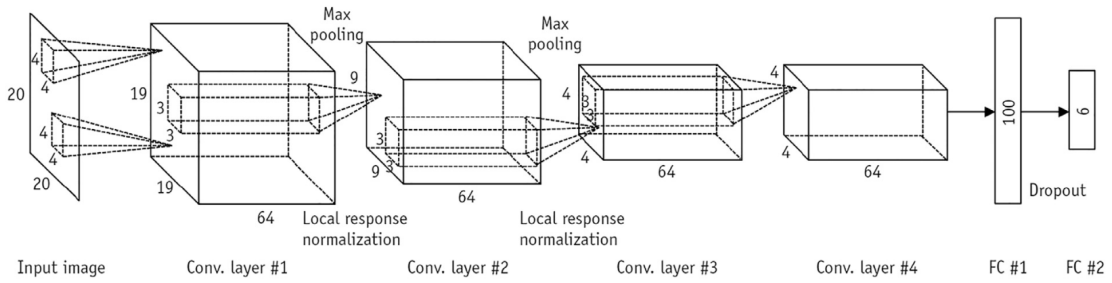

Figure 4.4: Architecture of CNNs [60].

The convolutional layer, primary building block of a CNN, applies specific filter operators, named convolutions, that merge two sets of information. The output is acquired through Kernels computing the product between the input and filter values [61, 62]. Moreover, the activation layer can be linear or non-linear. Their main function is to transform the input at a neuron to the output without any modifications. The pooling layer allows the reduction of the spatial size by adding the output of a neuron at one layer into a single neuron. The FC layer connects all the neurons in one layer to all the neurons in another layer and its main purpose is to make predictions based on the activations, that will then be used for classification. [62].

4.6 Application of the Methodology

The methodology used in this work was developed using Matlab® 2019b and FreeSurfer 7.1.1 software and it can be divided into 4 stages: (1) Pre-processing; (2) Feature Extraction; (3) Feature Selection and (4) Classification. The last step includes both classic Machine Learning and Deep Learning algorithms. This procedure is synthesized in Figure 4.5.

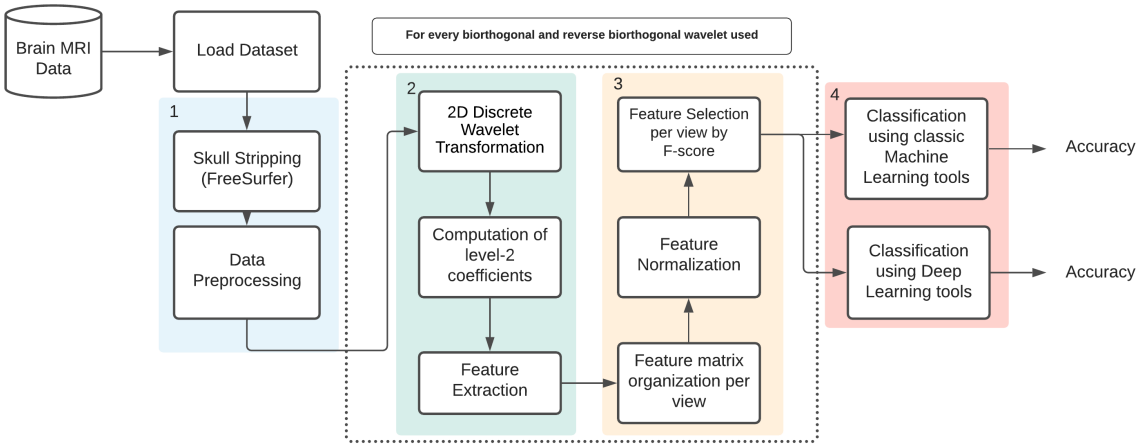

Figure 4.5: Diagram of the methodology used in the present work.

Firstly, the dataset have been uploaded to FreeSurfer 7.1.1 software (freely available online at https://surfer.nmr.mgh.harvard.edut) to execute the skull stripping process on the MR images. The resulting images were then loaded to Matlab® 2019b software. Each 3D subject data was decomposed into 2D slices comprising 3 different anatomical views – coronal, sagittal and axial. These images were treated with pre-processing techniques mentioned in section 4.2 - Median and Imadjust Filter - to remove noise and adjust the image intensity values. It is important to note that before the dataset download, these images had previously undergone determined correction steps, such as correction of image geometry distortion, image intensity non-uniformity, among others [63].

In the second stage, in order to discriminate the study groups, a set of features have been extracted from each MRI anotomical view. For this purpose, every image has been decomposed by the 2-D Discrete Wavelet Transform until level 2, according to the formulas 4.3, 4.4 and 4.5. In this step, the eight wavelets, mentioned in section 4.3.1.2, along with their subfamilies have been applied. A total of 9 features (contrast, correlation, energy, homogeneity, standard deviation, entropy, variance, mean and smoothness - consult Table 4.3) have been extracted from all the images resulting from the wavelet decomposition plus the original images per view. In parallel, it was employed the Kruskal-Wallis statistical test to determine if there are signifcant differences between the study groups. Thus, through this test, all 132 wavelets were analysed for every image, in the different views, and for the comparisons AD vs CN, AD vs MCI, MCI vs CN, and All vs All, to be able to understand amongst the total number of wavelets which ones had a greater discriminatory power. In this way, the five wavelets with the best results were chosen (Biorthogonal 1.1, Reverse Biorthogonal 1.1, Reverse Biorthogonal 1.3, Reverse Biorthogonal 1.5, and Reverse Biorthogonal 3.1). It was also verified that mean and smoothness did not present significant differences between subjects. Therefore, these features were not considered for this study. Figure 4.6 demonstrates some of the wavelets tested

and the number of p-values considered acceptable ($p < 0.05$, meaning that there are significant differences).

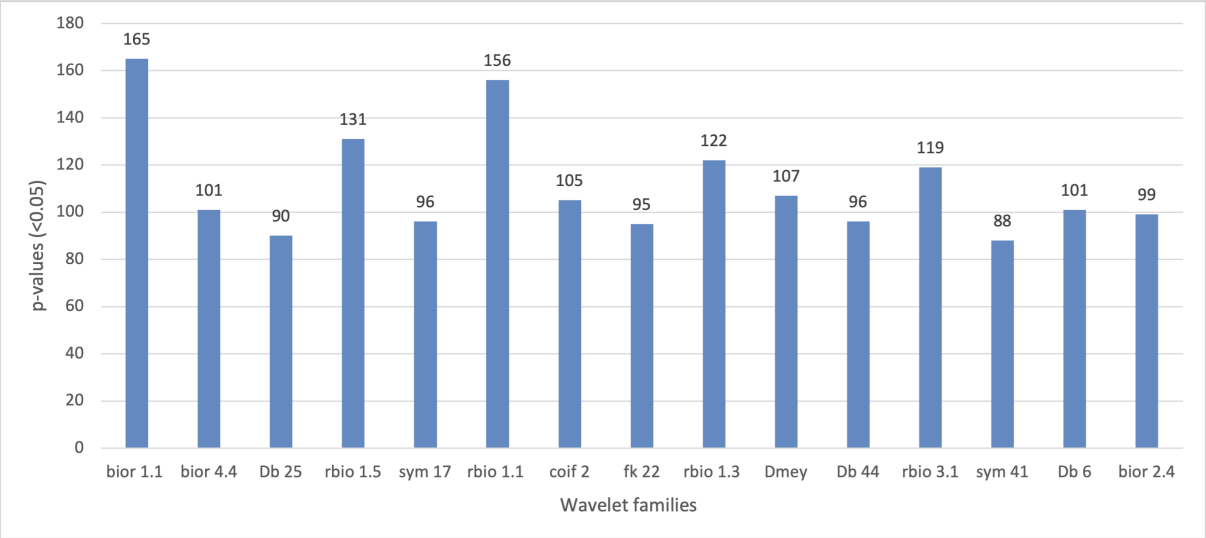

Figure 4.6: Overview of the wavelets tested and the total p-values obtained.

All the extracted information was organized in matrixes subject/feature per anatomical view. Additionally, a full matrix was created by the combination of the information extracted from the 3 anatomical views. Therefore, and to enhance the discriminative power of the metrics, an F-score algorithm was applied for feature selection, and the resulting features matrix was used as input in the Matlab Classification Learner APP with the intent of selecting the best feature combination according to the accuracy obtained by the following equation 4.11:

$$Accuracy = \frac{TP+TN}{TP+FN+FP+FN} \tag{4.11}$$

in which, TP, TN, FN and FP stand for true positive, true negative, false negative and false positive [64].

Through leave-one-out-cross validation, 25 classifiers have been trained to evaluate the best feature combination. For this purpose, all features were tested for all the comparisons made for each view (the best results are displayed in Table 4.4). In this way, it was found that the best feature combination for comparisons AD vs CN, AD vs MCI, MCI vs CN and All vs All include 80, 85, 90, 95 or 115 of the total features extracted. From table 4.4, it can be seen that these features are associated with the best classification results and amongst the majority of the comparisons made. Furthermore, the two best classifiers for each comparison have been chosen.

Table 4.4: Summary of the classic ML classification results.

	AD vs CN		AD vs MCI	
3 views	93.3%	115 ft	84.6%	80 ft
Coronal	88.9%	100 ft	87.7%	80, 95,140 ft
Sagittal	93.3%	35 ft	78.5%	6,170 ft
Axial	77.8%	45 ft	84.6%	85 ft
Best result	93.3%	115 ft,35 ft	87.7%	80,95,140 ft

	MCI vs CN		All vs All	
3 views	85.3%	120 ft	69.7%	25 ft
Coronal	88.2%	30,40,60,65,70,75,80,85,90 ft	75.3%	80,95,105,115 ft
Sagittal	82.4%	40 ft	65.2%	8,9,10,65,165,175 ft
Axial	82.4%	10 ft	69.7%	35,80ft
Best result	88.2%	30,40,60,65,70,75,80,85,90 ft	75.3%	80,95,105,115 ft

In this work, a Deep Learning algorithm was also implemented and comparisons with the Machine Learning classic algorithms were made. Therefore, the CNN was fed with the best feature combination determined by the ML tools within a leave-one-out-cross validation procedure. The best classification results are displayed in Table 4.5. The implemented CNN contained 6 layers – imageInputLayer, convolution2dLayer, reluLayer (activation layer), fullyConnectedLayer, softmaxLayer and classificationLayer (output layers). Firstly, the imageInputLayer feeds the CNN with a 2D image and then normalizes the data. Afterwards, the convolution2dLayer employs sliding convolutional filters to the image. Additionally, every element of this input suffers a threshold operation, by the reluLayer, setting values less than zero to zero. Then, the fullyConnectedLayer multiplies the image by a weight matrix and adds a bias vector. The softmaxLayer implements a softmax function to the image. Lastly, the classificationLayer calculates cross entropy loss for multi-class classifications with common exclusive classes [65]. It is important to refer that 2 and 3 fully connected layers were used for the binary and multi-class comparison, respectively. Moreover, three training algorithms were tested: adam, sgdm and rmsprop. It was verified that there were no differences in the accuracy values. In this way, the adam algorithm was chosen since it was the one programmed by default.

Additionally, a brief summary of the methodology is displayed in Figure 4.7.

Table 4.5: Summary of the DL classification results.

	AD vs CN		AD vs MCI	
Best result	82.2%	115 ft (coronal view)	75.4%	95 ft (3 views + coronal view)

	MCI vs CN		All vs All	
Best result	83.8%	85,90 ft (coronal view)	64.0%	80,85,95 ft (coronal view)

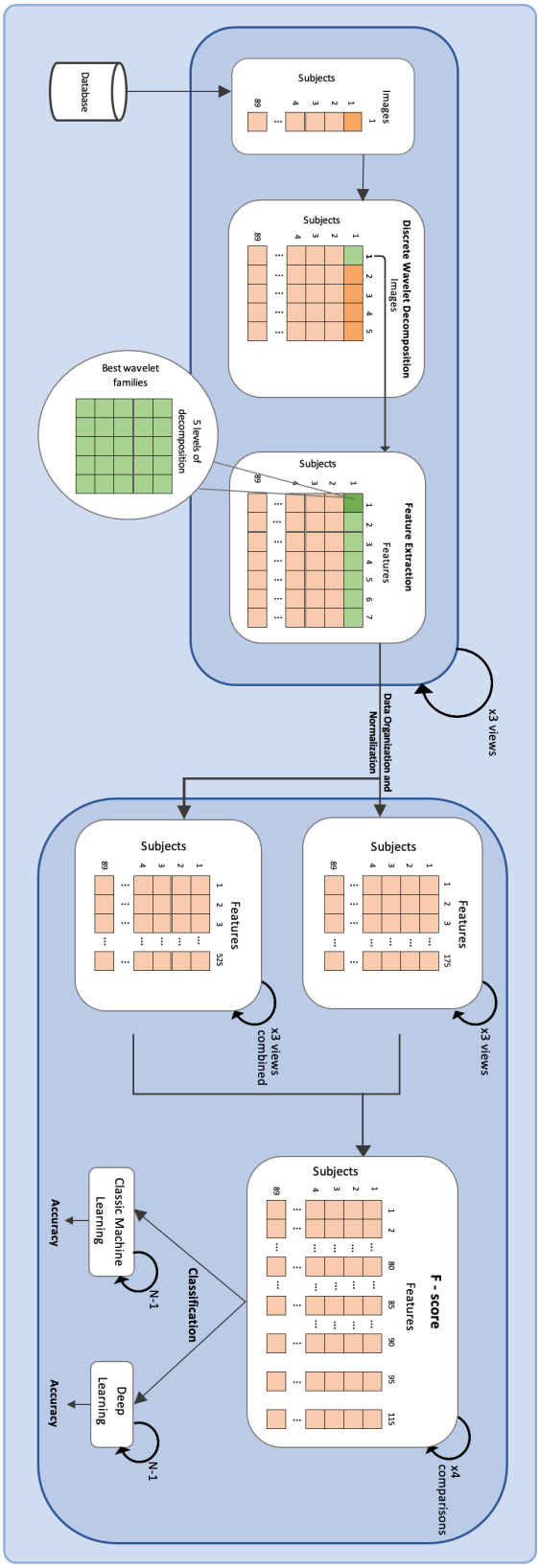

Figure 4.7: Diagram of the processes applied in the processing and classification phase.

CHAPTER 5

Discussion

In this chapter, the results obtained from classic Machine Learning and Deep Learning will be reported and compared. For both algorithms, binary and multi-class classifications were performed for the three study groups, each representing a different stage of the disease.

In terms of the comparison CN vs MCI, for the ML classic algorithms, the highest accuracy obtained was 88.2% by means of 80, 85 or 90 features. The classifiers that presented the best quality performance were Fine KNN and Subspace KNN. In turn, the DL algorithm presented a maximum accuracy of 83.8% by using 85 or 90 features. In both algorithms the coronal view was the one with the highest discriminative power.

Regarding the distinction of AD vs MCI, the ML classic algorithms obtained a highest accuracy of 87.7% with 80 or 95 features in the coronal view. Amongst all the classifiers tested, the Quadratic SVM classifier was associated with higher quality results for these study groups. In contrast, the DL algorithm achieved a maximum accuracy of 75.4% by the means of 95 features. Both the coronal view and the combination of the 3 anatomical views presented the same discriminatory power.

Concerning the classification of CN vs AD, the ML classic algorithms showed a maximum accuracy of 93.3% with 115 features in the 3 anatomical views. For this comparison, the best results were exhibited by the Bagged Trees classifier. In turn, the DL algorithm obtained a maximum accuracy of 82.2% with 115 features in the coronal view.

The multi-class classification of ALL vs ALL, revealed to be the one in which the algorithm experienced more difficulties to differentiate between groups. Thereby, both algorithms achieved a maximum accuracy lower than the previously obtained. Regarding the ML classic algorithms, it achieved a maximum accuracy of 75.3% in the coronal view by means of 80, 95 or 115 features. In this comparison, the classifier that achieved the most quality performance was the Subspace KNN classifier. In contrast, the DL algorithm accomplished a maximum accuracy of 64.0% with all 80, 85 or 95 features in the coronal view.

Amid the results obtained from the Machine Learning and Deep Learning algorithms, it is possible to state that the DL technique used (the CNN) did not outperformed the ML classic algorithms. The best results from both artificial intelligence algorithms are demonstrated in Table 5.1. Additionally, it was expected that overall, the comparison AD vs CN was the one achieving the best results, since these groups have more anatomical differences in the brain. This outcome was, certainly, verified with the ML classic algorithms.

Table 5.1: Summary of the results obtained by each technique.

	AD vs CN	**MCI vs CN**	**MCI vs AD**	**ALL vs ALL**
Machine Learning	93.3%	88.2%	87.7%	75.3%
Deep Learning	82.2%	83.8%	75.4%	64.0%

Upon the fact that the classic Machine Learning technique obtained the best results, the remaining analysis will be focused on this algorithm. Therefore, the extracted metrics that allowed the maximum accuracies to be achieved are exhibited in Table 5.2. The names attributed to these metrics are explained as follows: First is the variable name, followed by the wavelet family, and finally the level of decomposition (Variable_Wavelet_n). In which, n=1 corresponds to a level 2 2-D DWT for detail coefficients; n=2 to a level 2 2-D DWT for approximation coefficients; n=3 to a level 1 2-D DWT for detail coefficients; n=4 to a level 1 2-D DWT for approximation coefficients; and n=5 to the original image.

Overall, the coronal view obtained the best results. This is sustained by studies [66] and [67], and can be justified by the fact that it enables a clearer view to three of the most important tissues in AD (cerebral cortex, the ventricle, and the hippocampus). In this way, it is possible to sustain that the coronal view allows the best visualization of the differences in the various anatomical regions in the 3 different groups tested. Furthermore, despite all the features selected being within the highest accuracies, entropy and energy are emphasised. In what concerns the wavelet families, amongst the five best, the reverse biorthogonal 3.1 is outlined. This result is not in agreement with other studies. In these, the wavelets most commonly used are Dauchebis 4 and Haar wavelet [68]. Lastly, regarding the level of decomposition, it was found that the n=3 (level 1 2-D DWT for detail coefficients) should be highlighted.

Moreover, a comparison with other works in this field is fundamental to draw further conclusions. In this sense, Table 5.3 summarises the methodology and accuracies obtained by state of the art with the same database. Additionally, Table 5.4 displays the methodology and accuracies of imaging studies with other databases. Lastly, Table 5.5 presents the methodology and accuracies of non-imaging studies. The results are all rounded to the nearest integer number, and the methodology of studies [16], [17], [20] and [23] was previously described with more detail in the state of the art (section 2.4). As Tables 5.3, 5.4 and 5.5 clearly demonstrate, most studies distinguish the groups in a binary way

(CN vs AD, CN vs MCI and MCI vs AD), with only the method proposed in Rodrigues *et al.* [69] performing a multi-class classification (All vs All).

Compared with methods of diagnosing AD through sMRI using the same database (Table 5.3), in the CN vs MCI case, it outperformes the method developed inThapa *et al.* [17] by 9%. In contrast, when compared with the remaining comparisons studied (CN vs AD and MCI vs AD) it did not presented better outcomes. This considerable differences in classication accuracy may be due to the type of features extracted or the feature selection method applied.

With regard to AD diagnosis through other imaging techniques with the same database (Table 5.3), in the CN vs MCI case, it outperforms the FDG-PET method described in Liu *et al.* [70], by 9% of accuracy. Conversely, for the CN vs AD pair, it does not outperform the highest accuracy obtained, in this case by Amini *et al.* [20]. It is important to note that it is not a direct comparison of the different studies as the imaging techniques employed differ.

Compared with methods of diagnosing AD through sMRI using a different database (Table 5.4), the proposed work achieves the highest classification accuracies. In the CN vs AD case, it impressively outperforms the method employed in Qiu *et al.* [23] using AIBL, FHS and NACC databases by 6%, an impressive 16% and 11%, respectively. The remaining comparisons (CN vs MCI, MCI vs AD and All vs All) were not perform in this study. This results may be explained by the fact that no feature selection methods were applied in state of the art, enhancing the power of the F-score method. Conversly, compared with methods of diagnosing AD through other imaging techniques using a different database, it did not show better results. Once again it is not a direct comparison of the different studies as the databases used are different.

The proposed work was also compared with AD diagnosis through signal and biomarkers techniques (Table 5.5). When compared with the EEG method proposed in Rodrigues *et al.* [26] it did not outperformed the accuracies obtained. Since this work used a method that is not based on imaging thecniques, a direct comparison should be done carefully.

The work carried out relied on a small set of subjects, but the results achieved clearly demonstrate the potential of the metrics and techniques used. It is also possible to infer that the database used is usually associated with higher classification accuracies in the sMRI studies. These statements can be substantiated by the fact that overall, they outperformed state of the art classification accuracies in the binary classifications. The improvements obtained in CN vs AD, CN vs MCI and MCI vs AD indicate that the proposed work has a significant impact in the early detection of AD, playing an important role in delaying its evolution.

Table 5.2: Features selected by the F-score algorithm providing the best accuracies (Cont:Contrast; Corr:Correlation; Ener:Energy; Hom:Homogeneity; SD:Standard Deviation; Ent:Entropy; Var:Variance; r:rbio; b:bior).

AD vs MCI	**CN vs MCI**
Corr_r3.1_4; Corr_r1.1_3; Corr_b1.1_3;	Corr_r3.1_4; Corr_r1.1_3; Corr_b1.1_3;
Hom_r1.5_2; Cont_r1.5_2; Corr_r3.1_3;	Hom_r1.5_2; Cont_r1.5_2; Corr_r3.1_3;
Corr_r1.1_5; Corr_b1.1_5; Corr_r1.3_5;	Corr_r1.1_5; Corr_b1.1_5; Corr_r1.3_5;
Corr_r1.5_5; Corr_r3.1_5; Corr_r1.5_2;	Corr_r1.5_5; Corr_r3.1_5; Corr_r1.5_2;
Corr_r3.1_2; Ent_r3.1_2; Ent_r1.3_2;	Corr_r3.1_2; Ent_r3.1_2; Ent_r1.3_2;
Ent_r1.5_1; Cont_r1.1_3; Cont_b1.1_3;	Ent_r1.5_1; Cont_r1.1_3; Cont_b1.1_3;
Ent_r1.5_1; Corr_r1.3_3; Ent_r1.3_4;	Ent_r1.5_1; Corr_r1.3_3; Ent_r1.3_4;
Ent_r3.1_4; Ent_r1.1_2; Ent_b1.1_2;	Ent_r3.1_4; Ent_r1.1_2; Ent_b1.1_2;
Ent_r1.5_4; Hom_r1.5_4; Ent_r1.1_4;	Ent_r1.5_4; Hom_r1.5_4; Ent_r1.1_4;
Ent_b1.1_4; Cont_r3.1_4; Ener_r1.1_4;	Ent_b1.1_4; Cont_r3.1_4; Ener_r1.1_4;
Ener_b1.1_4; Hom_r1.1_3; Hom_b1.1_3;	Ener_b1.1_4; Hom_r1.1_3; Hom_b1.1_3;
Hom_r3.1_3; Ent_r1.1_5; Ent_b1.1_5;	Hom_r3.1_3; Ent_r1.1_5; Ent_b1.1_5;
Ent_r1.3_5; Ent_r1.5_5; Ent_r3.1_5;	Ent_r1.3_5; Ent_r1.5_5; Ent_r3.1_5;
Ener_r1.1_2; Ener_b1.1_2; Ener_r3.1_1;	Ener_r1.1_2; Ener_b1.1_2; Ener_r3.1_1;
Cont_r3.1_3; Ener_r1.5_4; Ener_r1.5_1;	Cont_r3.1_3; Ener_r1.5_4; Ener_r1.5_1;
Corr_r1.5_3; Hom_r1.5_1; Ener_r1.1_3;	Corr_r1.5_3; Hom_r1.5_1; Ener_r1.1_3;
Ener_b1.1_3; Ener_r1.5_2; Ener_r1.3_4;	Ener_b1.1_3; Ener_r1.5_2; Ener_r1.3_4;
Ent_r1.5_2; Cont_r1.3_1; Ener_r3.1_4;	Ent_r1.5_2; Cont_r1.3_1; Ener_r3.1_4;
Ener_r3.1_3; Hom_r3.1_1; Ener_r1.3_1;	Ener_r3.1_3; Hom_r3.1_1; Ener_r1.3_1;
Ener_r1.3_2; Corr_r1.1_4; Corr_b1.1_4;	Ener_r1.3_2; Corr_r1.1_4; Corr_b1.1_4;
Cont_r3.1_1; Hom_r1.3_1; Ent_r1.3_3;	Cont_r3.1_1; Hom_r1.3_1; Ent_r1.3_3;
Ener_r3.1_2; Ent_r3.1_3; Ent_r1.5_3;	Ener_r3.1_2; Ent_r3.1_3; Ent_r1.5_3;
Cont_r1.5_2; Hom_r3.1_4; Ent_r1.1_3;	Cont_r1.5_2; Hom_r3.1_4; Ent_r1.1_3;
Ent_b1.1_3; Ent_r1.1_1; Ent_b1.1_1;	Ent_b1.1_3; Ent_r1.1_1; Ent_b1.1_1;
Ener_r1.1_1; Ener_b1.1_1; Corr_r1.5_1;	Ener_r1.1_1; Ener_b1.1_1; Corr_r1.5_1;
Hom_r1.3_2; Cont_r1.1_1; Cont_b1.1_1;	Hom_r1.3_2; Cont_r1.1_1; Cont_b1.1_1;
Hom_r1.1_1; Hom_b1.1_1; Ener_r1.3_3;	Hom_r1.1_1; Hom_b1.1_1; Ener_r1.3_3;
Ent_r1.3_1; Ener_r1.1_5; Ener_b1.1_5;	Ent_r1.3_1; Ener_r1.1_5; Ener_b1.1_5;
Ener_r1.3_5; Ener_r1.5_5; Ener_r3.1_5;	Ener_r1.3_5; Ener_r1.5_5; Ener_r3.1_5;
Corr_r1.1_2; Corr_b1.1_2; SD_r3.1_1;	Corr_r1.1_2; Corr_b1.1_2; SD_r3.1_1
Var_r3.1_1; Ener_r1.5_3; Hom_r1.3_3;	
Hom_r1.5_3; Cont_r1.5_3	

AD vs CN	**ALL vs ALL**
Hom _r1.5_4; Hom_r1.5_2; Cont_r1.1_4; Cont_b1.1_4; Hom_r1.1_4; Hom_b1.1_4; Cont_r1.3_4; Hom_r1.3_4; Cont_r1.5_2; Cont_r1.1_5; Cont_b1.1_5; Cont_r1.3_5; Cont_r1.5_5; Cont_r3.1_5; Ent_r1.1_3; Ent_b1.1_3; Hom_r3.1_2; Cont_r3.1_2; Ent_r1.5_1; Hom_r1.3_2; Cont_r1.3_2; Ent_r1.3_1; Ent_r1.1_5; Ent_b1.1_5; Ent_r1.3_5; Ent_r1.5_5; Ent_r3.1_5; Ent_r1.3_3; Cont_r1.1_2; Cont_b1.1_2; Ent_r1.1_1; Ent_b1.1_1; Ener_r1.1_3; Ener_b1.1_3; Ent_r1.5_3; Hom_r1.1_5; Hom_b1.1_5; Hom_r1.3_5; Hom_r1.5_5; Hom_r3.1_5; Cont_r3.1_1; Hom_r3.1_1; Ener_r3.1_2; Hom_r1.1_3; Hom_b1.1_3; Ener_r3.1_3; Ener_r1.3_1; Ent_r3.1_3; Hom_r1.3_1; Ener_r3.1_4; Ener_r1.5_1; Ener_r1.1_1; Ener_b1.1_1; Ent_r1.3_4; Hom_r1.5_1; Ener_r1.5_2; Hom_r3.1_4; Ener_r3.1_1; Ener_r1.5_4; Ener_r1.1_4; Ener_b1.1_4; Hom_r1.5_3; Ener_r1.5_3; Hom_r1.1_1; Hom_b1.1_1; Hom_r3.1_3; Ent_r1.5_4; Ener_r1.3_4; Ener_r1.3_2; Ener_r1.1_2; Ener_b1.1_2; Ent_r1.3_2; Ent_r1.1_4; Ent_b1.1_4; Cont_r1.1_1; Cont_b1.1_1; Ener_r1.3_3; Cont_r1.5_4; Cont_r1.1_3; Cont_b1.1_3; Ent_r3.1_4; Hom_r1.3_3; Cont_r3.1_4; Ent_r3.1_1; Cont_r3.1_3; Ent_r1.5_2; Corr_r3.1_4; Ent_r1.1_2; Ent_b1.1_2; Hom_r1.1_2; Hom_b1.1_2; Var_r3.1_2; Corr_r3.1_1; Corr_r1.1_3; Corr_b1.1_3; Cont_r1.3_1; Cont_r1.5_1; Ent_r3.1_2; Cont_r1.5_3; Cont_r1.3_3; Corr_r1.3_1; Var_r3.1_3; SD_r3.1_3; Corr_r1.1_2; Corr_b1.1_2; Corr_r1.5_1; SD_r3.1_2; Ener_r1.1_5; Ener_b1.1_5	Corr_r3.1_4; Corr_r1.1_3; Corr_b1.1_3; Hom_r1.5_2; Cont_r1.5_2; Corr_r3.1_3; Corr_r1.1_5; Corr_b1.1_5; Corr_r1.3_5; Corr_r1.5_5; Corr_r3.1_5; Corr_r1.5_2; Corr_r3.1_2; Ent_r3.1_2; Ent_r1.3_2; Ent_r3.1_1; Cont_r1.1_3; Cont_b1.1_3; Ent_r1.5_1; Corr_r1.3_3; Ent_r1.3_4; Ent_r3.1_4; Ent_r1.1_2; Ent_b1.1_2; Ent_r1.5_4; Hom_r1.5_4; Ent_r1.1_4; Ent_b1.1_4; Cont_r3.1_4; Ener_r1.1_4; Ener_b1.1_4; Hom_r1.1_3; Hom_b1.1_3; Hom_r3.1_3; Ent_r1.1_5; Ent_b1.1_5; Ent_r1.3_5; Ent_r1.5_5; Ent_r3.1_5; Ener_r1.1_2; Ener_b1.1_2; Ener_r3.1_1; Cont_r3.1_3; Ener_r1.5_4; Ener_r1.5_1; Corr_r1.5_3; Hom_r1.5_1; Ener_r1.1_3; Ener_b1.1_3; Ener_r1.5_2; Ener_r1.3_4; Ent_r1.5_2; Cont_r1.3_1; Ener_r3.1_4; Ener_r3.1_3; Hom_r3.1_1; Ener_r1.3_1; Ener_r1.3_2; Corr_r1.1_4; Corr_b1.1_4; Cont_r3.1_1; Hom_r1.3_1; Ent_r1.3_3; Ener_r3.1_2; Ent_r3.1_3; Ent_r1.5_3; Cont_r1.5_1; Hom_r3.1_4; Ent_r1.1_3; Ent_b1.1_3; Ent_r1.1_1; Ent_b1.1_1; Ener_r1.1_1; Ener_b1.1_1; Corr_r1.5_1; Hom_r1.3_2; Cont_r1.1_1; Cont_b1.1_1; Hom_r1.1_1; Hom_b1.1_1; Ener_r1.3_3; Ent_r1.3_1; Ener_r1.1_5; Ener_b1.1_5; Ener_r1.3_5; Ener_r1.5_5; Ener_r3.1_5; Corr_r1.1_2; Corr_b1.1_2; SD_r3.1_1; Var_r3.1_1; Ener_r1.5_3; Hom_r1.3_3; Hom_r1.5_3; Cont_r1.5_3; Cont_r1.5_4; Cont_r1.3_3; Cont_r1.1_5; Cont_b1.1_5; Cont_r1.3_5; Cont_r1.5_5; Cont_r3.1_5; Cont_r1.3_2; Corr_r1.3_1; Hom_r1.1_5; Hom_b1.1_5; Hom_r1.3_5; Hom_r1.5_5; Hom_r3.1_5; Corr_r1.3_4; SD_r1.1_2; SD_b1.1_2; SD_r1.5_2; SD_r_1.3_2; SD_r1.1_4

Table 5.3: Comparison with previous works.

Study	Database	Exam Type	Features extracted	Best Classifier	Feature Selection	Accuracy
[16]	ADNI	sMRI	Voxels of ROIs	VAF-FS, Random Forest, XGBoost	ROIs	CN vs AD - 86% CN vs MCI - 72% MCI vs AD - 69%
[17]	ADNI	sMRI	MMSE, hippocampus left and right volume	SVM	Filter-based	CN vs AD - 99% CN vs MCI - 79% MCI vs AD - 91%
[23]	ADNI	sMRI	Disease probability maps	CNN	No feature selection method applied	CN vs AD - 83%
[20]	ADNI	fMRI	Average, standard deviation of cortical thickness, volume of cortical parceling, white matter, and surface area	CNN	PCA	CN vs AD - 97%
[71]	ADNI	PET	Voxel-wise intensity	CNN	No feature selection method applied	CN vs AD - 92%
[70]	ADNI	FDG-PET	Latent and generic features	CNN - BGRU	No feature selection method applied	CN vs AD - 91% CN vs MCI - 79%
Proposed work	ADNI	sMRI	Statisctical and textural features	KNN	F-score	CN vs AD - 93% CN vs MCI - 88% MCI vs AD - 88% All vs All - 75%

Table 5.4: Comparison with previous imaging works with different databases.

Study	Database	Exam Type	Features extracted	Best Classifier	Feature Selection	Accuracy
[23]	AIBL	sMRI	Disease probability maps	CNN	Not applied	CN vs AD - 87%
[23]	FHS	sMRI	Disease probability maps	CNN	Not applied	CN vs AD - 77%
[23]	NACC	sMRI	Disease probability maps	CNN	Not applied	CN vs AD - 82%
[72]	Thai University Hospital	PET	Mel-Frequency Cepstral Coefficients	SVM	Not applied	CN vs AD - 97%
Proposed work	ADNI	sMRI	Statisctical and textural features	KNN	F-score	CN vs AD - 93%
						CN vs MCI - 88%
						MCI vs AD - 88%
						All vs All - 75%

Table 5.5: Comparison with non-imaging works.

Study	Database	Exam Type	Features extracted	Best Classifier	Feature Selection	Accuracy
[26]	University Hospital Center of São João	EEG	Cepstral and Lacstral Distances	ANN	KW Test	CN vs ADM - 96%
						CN vs MCI - 98%
						MCI vs ADM-ADA - 94%
						All vs All - 96%
[69]	University Hospital Center of São João	EEG	Relative Power, Spectral Ratios, Maxima, Minima and Zero Crossing	ANN	KW Test	CN vs AD - 95%
						CN vs MCI - 77%
						MCI vs AD - 83%
						All vs All - 90%
[73]	IRCCS	EEG	Wavelet Coefficients	Decision Tree	Not applied	CN vs AD - 83%
						CN vs MCI - 92%
						MCI VS AD - 79%
[74]	Centre for Biomedical Technology	MEG	Measures of synchronization	Randomized 2-D CNN	Not applied	CN vs MCI - 91%
[75]	University Institute of Psychiatry	Biomarkers	$A\beta_{1-42}$/P-tau concentrations	ML	Not applied	CN vs AD - 83%
						MCI vs AD - 78%
Proposed work	ADNI	sMRI	Statisctical and textural features	KNN	F-score	CN vs AD - 93%
						CN vs MCI - 88%
						MCI vs AD - 88%
						All vs All - 75%

CHAPTER 6

Conclusions and future Perspectives

Conclusions

Alzheimer's Disease is one of the neurodegenerative diseases with the highest prevalence, affecting millions of people worldwide. Thus, this dissertation focuses on detecting AD in its early stages through the analysis of MRI images. Several features were used to perform this distinction and the results obtained revealed significant differences in the MRI images for all the comparisons made. Additionally, two different artificial intelligence algorithms, classic machine learning and deep learning, were employed. It was also disclosed that in this work, the ML classic algorithms presented significantly improved results. The distinction between the healthy control group and AD group was obtained with the highest accuracy, reinforcing that this disease causes extreme modifications in the human brain. Nonetheless, meaningful differences are also found between the distinction of AD and MCI groups and between healthy control and MCI groups. With this is mind, it is feasible to report that these findings are in conformity with the ones obtained in state of the art. In this sense, with these results, and despite the size and the unbalance present in the database (compromising the generalizability of the conclusions) it is possible to state that the features extracted are an important and accurate diagnostic tool for AD detection. Moreover, it can also be recognised that the accuracies obtained exceeded some of those presented in state of the art. In the CN vs MCI comparison, the proposed method, when compared with methods that use structural MRI, showed an increase in classification accuracy of 9%. Therefore, the potential of this work in the diagnosis of AD, mainly in its early stages, is reinforced. AD is an exceptionally relevant topic and, therefore, with several ongoing studies. In fact, a new Alzheimer's drug called Aduhelm, targeting the amyloid plaques that affect the underlying Alzheimer's disease process, has already been tested and recently approved by the Food and Drug Administration (FDA). In this way and combining new drugs with this intent with the proposed work, a powerful tool can be created, and AD could finally find a cure [76].

It should be noted that a Poster regarding this work was presented at the Affect, Personality and Embodied brain (APE2021) virtual conference [77].

Future Perspectives

With the aim of improving and consolidating the proposed tool, some proposals should be considered in the future:

- A larger database with the different balanced groups should be used, i.e., the groups should be similar in size.
- Create a graphical interface so that the algorithm can be implemented in clinical environment.
- Extract other features from the images and segment the hippocampus with the aim of assisting in the group's classification.
- Evaluate and try to distinguish Alzheimer's Disease from other forms of dementia, such as Lewy Body Disease, Vascular Dementia, among others.
- Adjust the CNN architecture structure to understand if it promotes better results. Attempting other deep learning technique could also be interesting.

Bibliography

[1] C. Qiu, M. Kivipelto, and E. von Strauss. "Epidemiology of Alzheimer's disease: occurrence, determinants, and strategies toward intervention". In: *Alzheimer's Disease and Mild Cognitive Impairment* 11.2 (June 2009), pp. 111–128. DOI: 10.31887/dcns.2009.11.2/cqiu.

[2] M. Figueira. *Manual de psiquiatria clínica*. Lisboa: Lidel, Edições Técnicas, 2014. ISBN: 978-9727579600.

[3] K. A. Johnson, N. C. Fox, R. A. Sperling, and W. E. Klunk. "Brain Imaging in Alzheimer Disease". In: *Cold Spring Harbor Perspectives in Medicine* 2.4 (Jan. 2012), a006213–a006213. DOI: 10.1101/cshperspect.a006213.

[4] P. Afonso. *Manual de psicofarmacologia na prática clínica*. Lisboa: Lidel, Edições Técnicas, 2018. ISBN: 978-989-752-337-3.

[5] A. Association. "2021 Alzheimer's disease facts and figures". In: *Alzheimer's & Dementia*. Vol. 17. 3. Wiley, Mar. 2021, pp. 327–406. DOI: 10.1002/alz.12328.

[6] R. Brookmeyer, E. Johnson, K. Ziegler-Graham, and H. M. Arrighi. "Forecasting the global burden of Alzheimer's disease". In: *Alzheimer's & Dementia* 3.3 (July 2007), pp. 186–191. DOI: 10.1016/j.jalz.2007.04.381.

[7] A. Kumar, A. Singh, and Ekavali. "A review on Alzheimer's disease pathophysiology and its management: an update". In: *Pharmacological Reports* 67.2 (Apr. 2015), pp. 195–203. DOI: 10.1016/j.pharep.2014.09.004.

[8] X. Zhang, Z. Fu, L. Meng, M. He, and Z. Zhang. "The Early Events That Initiate β-Amyloid Aggregation in Alzheimer's Disease". In: *Frontiers in Aging Neuroscience* 10 (Nov. 2018), p. 359. DOI: 10.3389/fnagi.2018.00359.

[9] *A Tour of Your Brain*. Visited on 20/04/2021. URL: https://www.alzinfo.org/brain/.

[10] L. G. Apostolova and P. M. Thompson. "Mapping progressive brain structural changes in early Alzheimer's disease and mild cognitive impairment". In: *Neuropsychologia* 46.6 (May 2008), pp. 1597–1612. DOI: 10.1016/j.neuropsychologia.2007.10.026.

[11] N. C. Fox, E. K. Warrinfton, P. A. Freeborough, P.Hartikainen, A. M. Kennedy, J. M. Stevens, and M. N. Rossor. "Presymptomatic hippocampal atrophy in Alzheimer's Disease: A longitudinal MRI Study". In: *Brain* 119.6 (Dec. 1996), pp. 2001–2006. DOI: 10.1093/brain/119.6.2001.

[12] I. Santana, D. Duro, R. Lemos, V. Costa, M. Pereira, M. R. Simões, and S. Freitas. "Mini-Mental State Examination: Avaliação dos Novos Dados Normativos no Rastreio e Diagnóstico do Défice Cognitivo". In: *Acta Médica Portuguesa* 29.4 (Apr. 2016), p. 240. DOI: 10.20344/amp.6889.

[13] W. M. van Oostveen and E. C. M. de Lange. "Imaging Techniques in Alzheimer's Disease: A Review of Applications in Early Diagnosis and Longitudinal Monitoring". In: *International Journal of Molecular Sciences* 22.4 (Feb. 2021), p. 2110. DOI: 10.3390/ijms22042110.

[14] N. N. Kulkarni, P. P. Rathod, and V. V. Nanavare. "The Role of Neuroimaging and Electroencephalogram in Diagnosis of Alzheimer Disease". In: *International Journal of Computer Applications* 167.11 (June 2017), pp. 40–46. DOI: 10.5120/ijca2017914435.

[15] C. Rosen, O. Hansson, K. Blennow, and H. Zetterberg. "Fluid biomarkers in Alzheimer's disease current concepts". In: *Molecular Neurodegeneration* 8.1 (2013), p. 20. DOI: 10.1186/1750-1326-8-20.

[16] E. Ruiz, J. Ramirez, J. M. Gorriz, J. Casillas, and the Alzheimer's Disease Neuroimaging Initiative. "Alzheimer's Disease Computer-Aided Diagnosis: Histogram-Based Analysis of Regional MRI Volumes for Feature Selection and Classification". In: *Journal of Alzheimer's Disease* 65.3 (Sept. 2018), pp. 819–842. DOI: 10.3233/JAD-170514.

[17] S. Thapa, P. Singh, D. K. Jain, N. Bharill, A. Gupta, and M. Prasad. "Data-Driven Approach based on Feature Selection Technique for Early Diagnosis of Alzheimer's Disease". In: *2020 International Joint Conference on Neural Networks (IJCNN)*. IEEE, July 2020, pp. 1–8. DOI: 10.1109/ijcnn48605.2020.9207359.

[18] R. Jain, N. Jain, A. Aggarwal, and D. J. Hemanth. "Convolutional neural network based Alzheimer's disease classification from magnetic resonance brain images". In: *Cognitive Systems Research* 57 (Oct. 2019), pp. 147–159. DOI: 10.1016/j.cogsys.2018.12.015.

[19] M. Hon and N. M. Khan. "Towards Alzheimer's disease classification through transfer learning". In: *2017 IEEE International Conference on Bioinformatics and Biomedicine (BIBM)*. IEEE, Nov. 2017, pp. 1166–1169. DOI: 10.1109/bibm.2017.8217822.

[20] M. Amini, M. M. Pedram, A. Moradi, and M. Ouchani. "Diagnosis of Alzheimer's Disease Severity with fMRI Images Using Robust Multitask Feature Extraction Method and Convolutional Neural Network (CNN)". In: *Computational and Mathematical Methods in Medicine* 2021 (Apr. 2021), pp. 1–15. DOI: 10.1155/2021/5514839.

[21] F. E. K. Al-Khuzaie, O. Bayat, and A. D. Duru. "Diagnosis of Alzheimer Disease Using 2D MRI Slices by Convolutional Neural Network". In: *Applied Bionics and Biomechanics* 2021 (Feb. 2021), pp. 1–9. DOI: 10.1155/2021/6690539.

[22] M. Liu, F. Li, H. Yan, K. Wang, Y. Ma, L. Shen, and M. Xu. "A multi-model deep convolutional neural network for automatic hippocampus segmentation and classification in Alzheimer's disease". In: *NeuroImage* 208 (Mar. 2020), p. 116459. DOI: 10.1016/j.neuroimage.2019.116459.

[23] S. Qiu, P. S. Joshi, M. I. Miller, C. Xue, et al. "Development and validation of an interpretable deep learning framework for Alzheimer's disease classification". In: *Brain* 143.6 (May 2020), pp. 1920–1933. DOI: 10.1093/brain/awaa137.

[24] K. Vaithinathan and L. Parthiban. "A Novel Texture Extraction Technique with T1 Weighted MRI for the Classification of Alzheimer's Disease". In: *Journal of Neuroscience Methods* 318 (Apr. 2019), pp. 84–99. DOI: 10.1016/j.jneumeth.2019.01.011.

[25] M. Maqsood, F. Nazir, U. Khan, F. Aadil, H. Jamal, I. Mehmood, and O. young Song. "Transfer Learning Assisted Classification and Detection of Alzheimer's Disease Stages Using 3D MRI Scans". In: *Sensors* 19.11 (June 2019), p. 2645. DOI: 10.3390/s19112645.

[26] P. M. Rodrigues, B. C. Bispo, C. Garrett, D. Alves, J. P. Teixeira, and D. Freitas. "Lacsogram: a New EEG Tool to Diagnose Alzheimer's Disease". In: *IEEE Journal of Biomedical and Health Informatics* 25.9 (Sept. 2021), pp. 3384–3395. DOI: 10.1109/jbhi.2021.3069789.

[27] P. Forouzannezhad, A. Abbaspour, C. Li, M. Cabrerizo, and M. Adjouadi. "A Deep Neural Network Approach for Early Diagnosis of Mild Cognitive Impairment Using Multiple Features". In: *2018 17th IEEE International Conference on Machine Learning and Applications (ICMLA)*. IEEE, 2018, pp. 1341–1346. DOI: 10.1109/icmla.2018.00218.

[28] M. Brown and R. Semelka. *MRI : Basic Principles and Applications*. Hoboken, N.J: Wiley-Liss, 2003. ISBN: 0-471-43310-1.

[29] R. A. Pooley. "Fundamental Physics of MR Imaging". In: *RadioGraphics* 25.4 (July 2005), pp. 1087–1099. DOI: 10.1148/rg.254055027.

[30] W. A. Worthoff, S. D. Yun, and N. J. Shah. "CHAPTER 1. Introduction to Magnetic Resonance Imaging". In: *Hybrid MR-PET Imaging*. Royal Society of Chemistry, 2018, pp. 1–44. DOI: 10.1039/9781788013062-00001.

[31] H. A. Ahmad, H. J. Yu, and C. G. Miller. "Medical Imaging Modalities". In: *Medical Imaging in Clinical Trials*. Springer London, 2013, pp. 3–26. DOI: 10.1007/978-1-84882-710-3_1.

[32] G. B. Frisoni, N. C. Fox, C. R. Jack, P. Scheltens, and P. M. Thompson. "The clinical use of structural MRI in Alzheimer disease". In: *Nature Reviews Neurology* 6.2 (Feb. 2010), pp. 67–77. DOI: 10.1038/nrneurol.2009.215.

[33] A. Chandra, G. Dervenoulas, and M. Politis. "Magnetic resonance imaging in Alzheimer's disease and mild cognitive impairment". In: *Journal of Neurology* 266.6 (Aug. 2018), pp. 1293–1302. DOI: 10.1007/s00415-018-9016-3.

[34] *Alzheimer's Disease Neuroimaging Initiative (ADNI) Data Sharing and Publication Policy*. Visited on 26/07/2021. URL: http://adni.loni.usc.edu/wp-content/uploads/how_to_apply/ADNI_DSP_Policy.pdf.

[35] L. Tan and J. Jiang. "Image Processing Basics". In: *Digital Signal Processing*. Elsevier, 2019, pp. 649–726. DOI: 10.1016/b978-0-12-815071-9.00013-0.

[36] *imadjust*. Visited on 15/09/2021. URL: https://www.mathworks.com/help/images/ref/imadjust.html.

[37] S. A. Villar, S. Torcida, and G. G. Acosta. "Median Filtering: A New Insight". In: *Journal of Mathematical Imaging and Vision* 58.1 (Dec. 2016), pp. 130–146. DOI: 10.1007/s10851-016-0694-0.

[38] I. S. Isa, S. N. Sulaiman, M. Mustapha, and S. Darus. "Evaluating Denoising Performances of Fundamental Filters for T2-Weighted MRI Images". In: *Procedia Computer Science* 60 (2015), pp. 760–768. DOI: 10.1016/j.procs.2015.08.231.

[39] S. Chaplot, L. M. Patnaik, and N. R. Jagannathan. "Classification of magnetic resonance brain images using wavelets as input to support vector machine and neural network". In: *Biomedical Signal Processing and Control* 1.1 (Jan. 2006), pp. 86–92. DOI: 10.1016/j.bspc.2006.05.002.

[40] D. R. Nayak, R. Dash, and B. Majhi. "Brain MR image classification using two-dimensional discrete wavelet transform and AdaBoost with random forests". In: *Neurocomputing* 177.C (Feb. 2016), pp. 188–197. DOI: 10.1016/j.neucom.2015.11.034.

[41] D. Zhang. "Wavelet Transform". In: *Texts in Computer Science*. Springer International Publishing, 2019, pp. 35–44. DOI: 10.1007/978-3-030-17989-2_3.

[42] R. Gonzalez and R. Woods. *Digital Image Processing*. New York, NY: Pearson, 2018. ISBN: 9780133356724.

[43] P. Moulin. "Multiscale Image Decompositions and Wavelets". In: *The Essential Guide to Image Processing*. Elsevier, 2009, pp. 123–142. DOI: 10.1016/b978-0-12-374457-9.00006-8.

[44] M. Misiti, Y. Misiti, G. Oppenheim, and J.-M. Poggi. *Wavelet Toolbox User's Guide*. Ed. by MathWorks. 2021.

[45] M. Nielsen. "On the Construction and Frequency Localization of Finite Orthogonal Quadrature Filters". In: *Journal of Approximation Theory* 108.1 (Jan. 2001), pp. 36–52. DOI: 10.1006/jath.2000.3514.

[46] O. Rashid, A. Amin, and M. R. Lone. *Performance Analysis of DWT Families*. Piscataway, New Jersey: IEEE, 2020. ISBN: 978-1-7281-7089-3.

[47] S. K. P.S and D. V.S. "Extraction of Texture Features using GLCM and Shape Features using Connected Regions". In: *International Journal of Engineering and Technology* 8.6 (Dec. 2016), pp. 2926–2930. DOI: 10.21817/ijet/2016/v8i6/160806254.

[48] *graycomatrix*. Visited on 15/09/2021. URL: https://www.mathworks.com/help/images/ref/graycomatrix.html.

[49] N. Sevani, I. Hermawan, and W. Jatmiko. "Feature Selection based on F-score for Enhancing CTG Data Classification". In: *2019 IEEE International Conference on Cybernetics and Computational Intelligence (CyberneticsCom)*. IEEE, 2019, pp. 18–22. DOI: 10.1109/cyberneticscom.2019.8875656.

[50] J. Li, K. Cheng, S. Wang, F. Morstatter, R. P. Trevino, J. Tang, and H. Liu. "Feature Selection". In: *ACM Computing Surveys* 50.6 (Jan. 2018), pp. 1–45. DOI: 10.1145/3136625.

[51] G. Bonaccorso. *Machine Learning Algorithms*. Packt, July 2017, p. 360. ISBN: 9781785889622.

[52] D. Bhargava, S. Vyas, and A. Bansal. "Comparative analysis of classification techniques for brain magnetic resonance imaging images". In: *Advances in Computational Techniques for Biomedical Image Analysis*. Elsevier, 2020, pp. 133–144. DOI: 10.1016/b978-0-12-820024-7.00007-4.

[53] S. Huang, N. Cai, P. Pacheco, S. Narandes, Y. Wang, and W. Xu. "Applications of Support Vector Machine (SVM) Learning in Cancer Genomics". In: *Cancer Genomics & Proteomics* 15.1 (Jan. 2018), pp. 41–51. DOI: 10.21873/cgp.20063.

[54] H. P. Bhavsar and M. Panchal. "A Review on Support Vector Machine for Data Classification". In: 2012.

[55] V. Wasule and P. Sonar. "Classification of brain MRI using SVM and KNN classifier". In: *2017 Third International Conference on Sensing, Signal Processing and Security (ICSSS)*. IEEE, May 2017, pp. 218–223. DOI: 10.1109/ssps.2017.8071594.

[56] S. M. Ayyad, A. I. Saleh, and L. M. Labib. "Gene expression cancer classification using modified K-Nearest Neighbors technique". In: *Biosystems* 176 (Feb. 2019), pp. 41–51. DOI: 10.1016/j.biosystems.2018.12.009.

[57] A. Singh, A. Yadav, and A. Rana. "K-means with Three different Distance Metrics". In: *International Journal of Computer Applications* 67.10 (Apr. 2013), pp. 13–17. DOI: 10.5120/11430-6785.

[58] O. Sagi and L. Rokach. "Ensemble learning: A survey". In: *WIREs Data Mining and Knowledge Discovery* 8.4 (Feb. 2018). DOI: 10.1002/widm.1249.

[59] X. Dong, Z. Yu, W. Cao, Y. Shi, and Q. Ma. "A survey on ensemble learning". In: *Frontiers of Computer Science* 14.2 (Aug. 2019), pp. 241–258. DOI: 10.1007/s11704-019-8208-z.

[60] F. F. Ting, Y. J. Tan, and K. S. Sim. "Convolutional neural network improvement for breast cancer classification". In: *Expert Systems with Applications* 120 (Apr. 2019), pp. 103–115. DOI: 10.1016/j.eswa.2018.11.008.

[61] S. M. Anwar, M. Majid, A. Qayyum, M. Awais, M. Alnowami, and M. K. Khan. "Medical Image Analysis using Convolutional Neural Networks: A Review". In: *Journal of Medical Systems* 42.11 (Oct. 2018), pp. 1–13. DOI: 10.1007/s10916-018-1088-1.

[62] A. Dhillon and G. K. Verma. "Convolutional neural network: a review of models, methodologies and applications to object detection". In: *Progress in Artificial Intelligence* 9.2 (Dec. 2019), pp. 85–112. DOI: 10.1007/s13748-019-00203-0.

[63] *ADNI: MRI Analysis*. Visited on 26/07/2021. URL: http://adni.loni.usc.edu/methods/mri-tool/mri-analysis/#mri-pre-processing-container.

[64] V. Bairagi. "EEG signal analysis for early diagnosis of Alzheimer disease using spectral and wavelet based features". In: *International Journal of Information Technology* 10.3 (Apr. 2018), pp. 403–412. DOI: 10.1007/s41870-018-0165-5.

[65] *trainingOptions*. Visited on 3/09/2021. URL: https://www.mathworks.com/help/deeplearning/ug/list-of-deep-learning-layers.html.

[66] M. Raza, M. Awais, W. Ellahi, N. Aslam, H. Nguyen, and H. Le-Minh. "Diagnosis and monitoring of Alzheimer's patients using classical and deep learning techniques". In: *Expert Systems with Applications* 136 (Dec. 2019), pp. 353–364. DOI: 10.1016/j.eswa.2019.06.038.

[67] F. Ren, C. Yang, Q. Qiu, N. Zeng, C. Cai, C. Hou, and Q. Zou. "Exploiting Discriminative Regions of Brain Slices Based on 2D CNNs for Alzheimer's Disease Classification". In: *IEEE Access* 7 (2019), pp. 181423–181433. DOI: 10.1109/access.2019.2920241.

[68] D. Jaramillo, I. Rojas, O. Valenzuela, I. García, and A. Prieto. "Advanced systems in medical decision-making using intelligent computing. Application to magnetic resonance imaging". In: *The 2012 International Joint Conference on Neural Networks (IJCNN)*. 2012, pp. 1–8. DOI: 10.1109/IJCNN.2012.6252575.

[69] P. M. Rodrigues, D. R. Freitas, J. P. Teixeira, D. Alves, and C. Garrett. "Electroencephalogram Signal Analysis in Alzheimer's Disease Early Detection". In: 7.1 (Jan. 2018), pp. 40–59. DOI: 10.4018/ijrqeh.2018010104.

[70] M. Liu, D. Cheng, and W. Y. and. "Classification of Alzheimer's Disease by Combination of Convolutional and Recurrent Neural Networks Using FDG-PET Images". In: 12 (June 2018). DOI: 10.3389/fninf.2018.00035.

[71] D. Cheng and M. Liu. "Classification of Alzheimer's Disease by Cascaded Convolutional Neural Networks Using PET Images". In: *Machine Learning in Medical Imaging*. Springer International Publishing, 2017, pp. 106–113. DOI: 10.1007/978-3-319-67389-9_13.

[72] J. Panyavaraporn and P. Horkaew. "Classification of Alzheimer's Disease in PET Scans using MFCC and SVM". In: *International Journal on Advanced Science, Engineering and Information Technology* 8 (2018), pp. 1829–1835.

[73] G. Fiscon, E. Weitschek, A. Cialini, G. Felici, P. Bertolazzi, S. D. Salvo, A. Bramanti, P. Bramanti, and M. C. D. Cola. "Combining EEG signal processing with supervised methods for Alzheimer's patients classification". In: 18.1 (2018). DOI: 10.1186/s12911-018-0613-y.

[74] M. Lopez-Martin, A. Nevado, and B. Carro. "Detection of early stages of Alzheimer's disease based on MEG activity with a randomized convolutional neural network". In: 107 (July 2020), p. 101924. DOI: 10.1016/j.artmed.2020.101924.

[75] O. V. Forlenza, M. Radanovic, L. L. Talib, I. Aprahamian, B. S. Diniz, H. Zetterberg, and W. F. Gattaz. "Cerebrospinal fluid biomarkers in Alzheimer's disease: Diagnostic accuracy and prediction of dementia". In: 1.4 (Oct. 2015), pp. 455–463. DOI: 10.1016/j.dadm.2015.09.003. URL: https://doi.org/10.1016/j.dadm.2015.09.003.

[76] O. of the Commissioner. *FDA Grants Accelerated Approval for Alzheimer's Drug*. Visited on 10/09/2021. URL: https://www.fda.gov/news-events/press-announcements/fda-grants-accelerated-approval-alzheimers-drug.

[77] J. Silva and P. M. Rodrigues. "Machine learning models for automatic detection of Alzheimer's Disease using Magnetic Resonance Imaging (MRI)". In: *Proceedings of Affect, Personality and the Embodied Brain Conference "APE2020"* (2021), p. 34.